Explaining the FLASH effect

Investigating the Oxygen Hypothesis of the Proton FLASH Effect in Zebrafish

Master Thesis

M.J. de Groot

Delft University of Technology

TU Delft

Explaining the FLASH effect

Investigating the Oxygen Hypothesis of the Proton FLASH Effect in Zebrafish

by

M.J. de Groot

To obtain the degree of

Master of Science

At the Delft University of Technology, faculty of Applied Sciences

Student Number:	4491866
Supervisor:	Elizabeth Carroll
Supervisor:	Zoltán Perkó
Institution:	Delft University of Technology
Place:	Faculty of Applied Sciences, HollandPTC, Delft
Project Duration:	March, 2021 - October, 2022

Cover: Max-projected fluorescence microscopy image of a FLASH-irradiated zebrafish

TU Delft

Acknowledgments

This thesis has been a long and at difficult project, in ways that at times even exceeded the academic dimension. It could not have existed without the help of many dear people. I thank my fellow students, Alexandra van Dongen and Quincy Buuron. Laura Maddalena, for always being flexible and available for help. Huma Safdar, Han van der Linden and Johan van der Cingel, for practical assistance. And of course my supervisors, Elizabeth Carrol and Zoltán Perkó.

M.J. de Groot
Delft, September 2022

Abstract

This thesis investigates the tissue sparing effect of FLASH (>40 Gy/s) radiation, as opposed to CONV (conventional, dose rates typically between 0.01-0.1 Gy/s) radiation. We irradiated zebrafish embryos (4 days past fertilisation) with 116 MeV protons. The aim was (1) to measure the effect, and (2) if the effect were significant, see whether it depended on the oxygen concentration in the tissue, as the oxygen depletion hypothesis (a popular theory on the underlying mechanics of the FLASH effect) predicts. We irradiated embryos with either FLASH or CONV, where a possible FLASH effect would reduce toxicity of the FLASH radiation. We did the same for zebrafish which were deliberately put in a hypoxic condition prior to irradiation. In that case, the depletion hypothesis would predict that the difference between FLASH and CONV disappears. Our biomarkers for radiobiological damage were the survival rate and γ-H2AX foci formation. In our experimental conditions, the radiation effect on the survival rate was eclipsed by other factors which could not be isolated. We did confirm the possibility of using γ-H2AX foci formation as a marker for radiobiological damage in full-body irradiated zebrafish embryos. There were individual samples that showed clear and localised specific γ-H2AX signal, but these were too scarce and the signal was too inconsistent across samples to gather meaningful statistics. This was most often caused by limited antibody penetration in the embryo. We were therefore unable to draw conclusions about the FLASH effect. Better and more consistent antibody penetration, e.g. by longer digestion in collagenase before antibody staining, could change this in the future.
We further custom-built and validated a hypoxic aquarium to produce hypoxic zebrafish tissue, as well as a computational model of the irradiation setup to simulate the dose distribution in the zebrafish container. We found the dose distribution to be sufficiently homogeneous for our experiment, at least 91.47% uniform for CONV and 90.72% uniform for FLASH.

Contents

List of Figures

1 Introduction

Cancer remains the second leading cause of death worldwide, accounting for approximately one in six deaths in 2020 [1]. Around half of all cancer treatments include at least some form of radiotherapy [2]. The paradigmatic challenge of radiotherapy is to improve the therapeutic ratio, i.e. to maximally damage the tumour while minimally damaging the healthy tissue surrounding it. A recent innovation to minimize damage to healthy tissue is FLASH radiotherapy, radiotherapy with dose rates exceeding 40 Gy/s, multiple orders of magnitude above CONV (conventional) radiotherapy [3]. The same dose of ionizing radiation seems less toxic to healthy tissue when administered very quickly, rather than slowly [4] [5] [6] [7] [8] [9]. This tissue sparing effect is commonly called the *FLASH effect*. Ultimately, FLASH could allow for higher doses in tumor treatment without the added toxicity leading to a worse patient outcome, or for administering the same dose with less negative side effects.

There is a lot of research still to be done on both the FLASH effect and its underlying mechanism. There is little insight and no scientific consensus on the reason why FLASH would be less toxic than other radiotherapy. Radiation experiments can vary greatly in type of radiation, animal model, and endpoint (e.g. embryo length, survival, foci formation of a certain antibody). Each combination of radiation type, animal model and endpoint is a new situation, where the results of the experiment might not be predicted by the results of a slightly different combination. The absence or presence of the FLASH effect in specific situations can ultimately help us understand the underlying principles that cause it, which would contribute to better clinical application.

The first aim of this thesis is to investigate the FLASH effect for 116 MeV proton irradiation in the zebrafish animal model, with two endpoints: mortality and γ-H2AX foci formation, an antibody that binds to double-straned DNA breaks, which are caused by ionizing radiation. There have been a few other publications on the proton FLASH effect [10], of which most have used *in vitro* animal models, i.e. cells in a petri dish rather than in a live organism (*in vivo*) [8] [11] [12] [13] [14]. *In vivo* experiments have been conducted mostly on mice [5] [6] [15] [16]. The research most similar to this thesis investigated the proton FLASH effect in zebrafish, but with other endpoints (i.e. survival, embryo length and oedema development around the heart) [7]. They did not find a significant FLASH effect.

A second aim of this thesis is to investigate a popular hypothesis of the mechanism underlying the FLASH effect, the oxygen depletion hypothesis. A much more detailed, comprehensive and annotated description of the oxygen depletion hypothesis can be found in Section 2.5, but it can be adequately summarized as follows: hypoxic tissue tends to be more radioresistant than highly oxygenated tissue, and high dose rate radiation would deplete molecular oxygen quicker than the circulatory system can replenish it. This leads to the irradiated tissue becoming more hypoxic and therefore more radioresistant. This tissue sparing effect would apply less to tumors than to healthy tissue, because tumors, often not as connected to the circulatory system as 'regular' organs, already tend to be hypoxic anyway. Therefore, the hypothesis would also neatly explain why the reduced toxicity is not as relevant for tumor tissue. While there is evidence for an oxygen-dependent FLASH effect [17] [18], recently the scientific community seems to doubt that oxygen depletion could be the entire or even the chief explanation [19]

[20].

These aims are united in the following research question:

Is there an oxygen dependent FLASH effect in proton-irradiated zebrafish?

To answer this question we devised an experiment that includes four groups, each receiving a different radiation treatment. Two groups have their tissue deliberately made hypoxic even prior to the irradiation, we call these hypoxic groups. Groups with a normal molecular oxygen concentration before irradiation we call normoxic. Each of the hypoxic and normoxic groups is irradiated either by CONV or FLASH radiation, creating these four treatments:

1. Normoxic, CONV irradiated
2. Normoxic, FLASH irradiated
3. Hypoxic, CONV irradiated
4. Hypoxic, FLASH irradiated

Were there to be a FLASH effect, we would expect the FLASH irradiated groups to be less damaged by the radiation than the CONV irradiated groups. If this FLASH effect is furthermore *oxygen dependent*, we expect this sparing effect to be less significant between the hypoxic groups than between the normoxic groups. The oxygen depletion hypothesis would entail that if the tissue is already hypoxic, FLASH should not have a tissue-sparing advantage over CONV. In this thesis, we applied these four treatments using different doses of radiation, and tried to quantify the damage with our chosen biomarkers.
To conduct all the experiments, this thesis project also included custom-building and validating a hypoxic aquarium to create embryos with hypoxic tissue. We furthermore devised the irradiation setup together with the radiation technicians of HollandPTC, and simulated the dose distribution in the embryo container to make sure it was sufficiently homogeneous in our experimental conditions.

This thesis report will further feature a theory chapter that elaborates on proton radiation, the FLASH effect, the oxygen depletion hypothesis, and other concepts the reader should be familiar with to understand the rest of the thesis. Chapter 3 explains all the models, experimental setups and protocols used during the project. The results are displayed in chapter 4, conclusions and recommendations made in chapter 5. Code to recreate the computational model and data analysis can be found in appendices A, B and C.

2

Theory

2.1. Proton Radiation

Proton therapy is distinct from other radiation therapies by the dose deposition as a function of the distance travelled through a medium, its depth-dose profile. Figure 2.1 shows the depth-dose profiles of photons, electrons, protons and carbon ions. When compared to photons and electrons, which are the most conventional types of radiation in the clinic, the entrance dose deposited by protons is very low. The bulk of the dose is deposited in a small window, called the Bragg peak. Consequently, proton irradiation in many cases allows for a higher therapeutic ratio (the ratio between the likelihood of tumor control and the likelihood of healthy tissue damage), as dose deposition is low before and after the Bragg peak, which can be aimed at the tumor. This is especially the case when the tumor lies deeper in the body, or is surrounded by delicate organs.

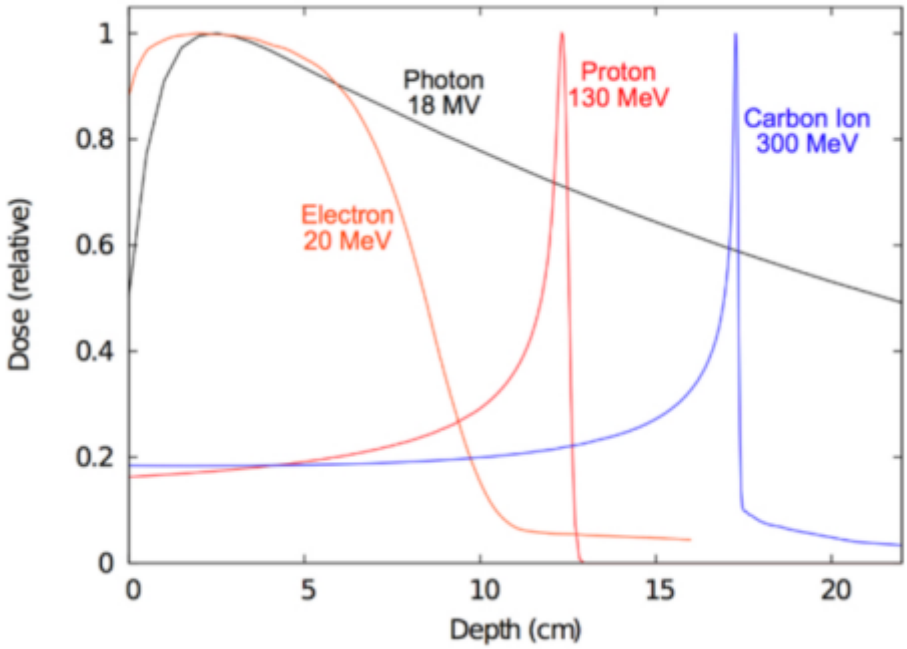

Figure 2.1: Dose distributions as a function of depth in water shown for various clinical radiation beams [21]

2.1.1. The Spread Out Bragg Peak

The location of the Bragg peak depends on the energy of the incoming proton. Higher energy protons will experience their Bragg peak deeper into the medium. This means that a proton beam with multiple

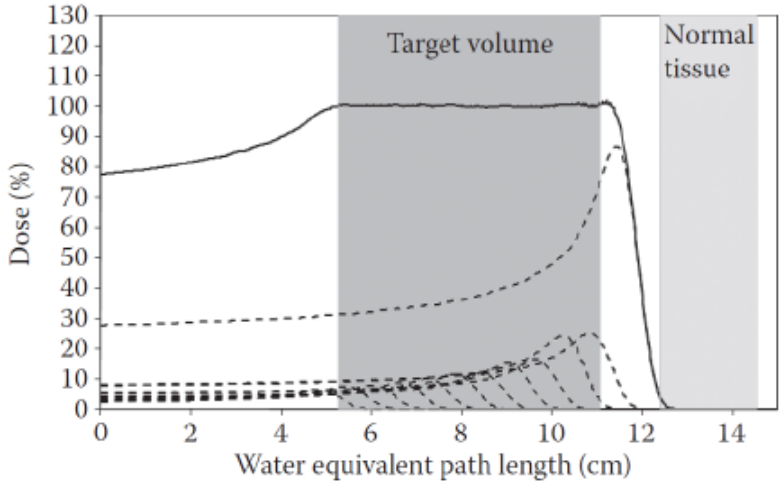

Figure 2.2: Different 'pristine' Bragg curves from protons with different energies, with different weights, producing an SOBP. [22]

energies will produce a depth-dose figure that is the weighted sum of the Bragg peak for each individual energy. The right proton distribution will produce a plateau where the dose is mostly homogeneous, a Spread Out Bragg Peak (SOBP). The energy spectrum of a mono-energetic proton beam can be manipulated to produce an SOBP in the medium by a ridge filter (shown in figure 2.3, which consists of an array of pyramid-shaped plastic pins, ridges). Because of the shape, each part of the beam experiences a different path-length through the filter, the energies are modulated by the plastic's stopping power: some protons have their energies reduced more than others.

Normally, energy spectra of pencil beams (such as at HollandPTC) are modulated by movable degraders or range modulator wheels, which are more modern methods [23]. However, with FLASH radiotherapy, ridge filters seem to make a comeback. As static components, they are not bothered by the much stricter time constraints that FLASH dose rates (with associated treatment lengths in the order of milliseconds) impose on components in the setup [24]. Because our achievable dose remained sufficiently high, we ended up choosing to scatter the initial pencil beam to a larger passive scattering field anyway, using the passive scattering setup described in 3.4.

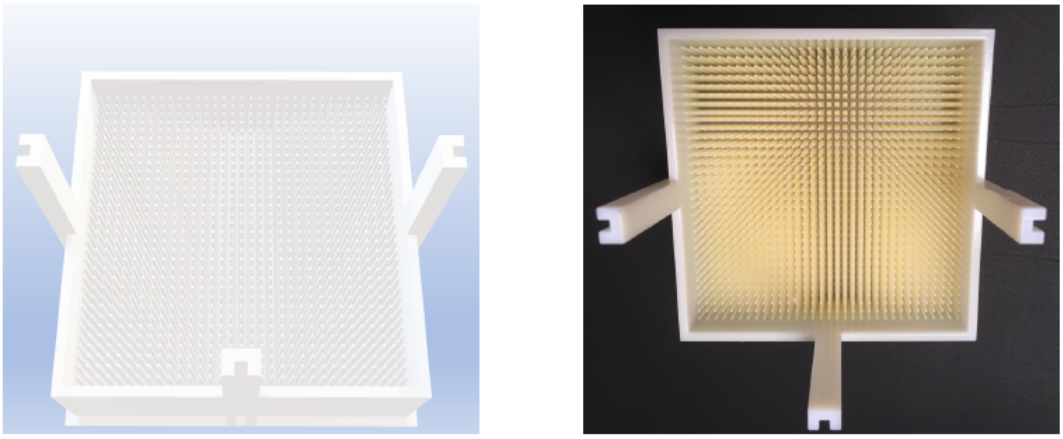

Figure 2.3: Ridge filter used in the simulations and in the actual measurement. In (a) the 3D model by GSI, in (b) a picture of the filter used during irradiation. [23]

2.1.2. Interactions

Most of the energy transfer from an incoming proton to other particles comes from electromagnetic interaction of the proton with atomic electrons. The attraction of atomic electrons reduces the proton's kinetic energy. The rate at which this slowing down of the proton happens, is called the stopping power. Because the interaction between the proton and and an electron becomes increasingly longer as the proton slows down, the stopping power increases as the proton's kinetic energy decreases, further increasing the stopping power. This mechanism causes the Bragg peak, where a proton suddenly deposits all of its energy. The stopping power (S) experienced by a charged particle, i.e. the energy loss per distance travelled ($-\frac{dE}{dx}$), was described by Hans Bethe and Felix Bloch in 1933 as [25]:

$$S = -\frac{dE}{dx} = \frac{4\pi e^4 Z_t Z_p^2 \rho}{m_e v^2} \left[\ln \frac{2m_e v^2}{I} - \ln\left(1-\beta^2\right) - \beta^2 \right], \tag{2.1}$$

where Z_m and Z_p correspond to the mass numbers of the medium and the particle, ρ to the material density, m_e to electron mass, e to electron charge, v to the particle velocity, I to the mean excitation potential, and $\beta = v/c$. One will often find versions of the formula with extra terms between the square brackets to correct for perturbations caused by quantum mechanical effects, but these are only significant for very low energies, orders of magnitude from typical radiotherapy energies (in our case 116 MeV). Indeed, we see that the energy loss is inversely proportional to the velocity squared.

Other interactions include Coulomb scattering off of other nuclei, which changes the propagation angle of the proton. As a consequence, every proton beam propagating through a medium with some scattering power will soon have a Gaussian angular distribution, as is described by the Highland formula [26]. Section 3.8.2 shows how we model the angular distribution of our proton beams. Lastly, protons can undergo nuclear interactions with other nuclei. Although not as influential as stopping and scattering, which are electromagnetic interactions, these do happen and should be taken into account when performing dose calculations. These interactions can produce neutrons that can administer dose outside the targeted area. Also, reaction products can be radioactive [27].

2.2. FLASH Radiotherapy

In the quest for radiotherapy that better spares healthy tissue, 'FLASH'-irradiation might be a promising new form of radiotherapy [28]. FLASH-radiotherapy is radiotherapy with an ultra-high dose rate, and is often juxtaposed to radiotherapy with conventional (i.e. lower) dose rates (CONV). Dose rates above 40 Gray per second are generally considered FLASH dose rates [3]. This is multiple orders of magnitude higher than CONV dose rates, which are around 1 Gray per minute. FLASH is not yet used in the clinic, but clinical trials on humans have taken place [29].

2.3. The FLASH Effect

Since experimenting with FLASH therapy has started, researches have demonstrated some tissue-sparing effects, which are referred to as the FLASH-effect. The first discovery of the FLASH effect is credited to a 2014 paper [30], which demonstrated reduced lung toxicity in mice while the damage to the tumor remained equivalent to CONV-radiotherapy. There is also evidence for reduced cell senescence, reduced expression of a pro-inflammatory marker [8], reduced pericardial edema [7], increased cell survival [17], and even long-term neurocognitive benefits, also in mice [9].

There are also practical advantages to FLASH irradiation. Because the treatment time is radically decreased, interference with the irradiation plan by minor motion of the patient or unpredictable positional variations within the body that happen over time (mainly due to bowel activity), are reduced. This would allow for smaller margins during treatment planning. Furthermore, shorter treatment times and possibly fewer treatment fractions will be more convenient for the patient.

2.4. Radiobiological Damage

To hypothesize about the underlying mechanism of the FLASH-effect (as we will in section 2.5), we need to have an idea of how radiation causes biological damage. As mentioned in Section 2.1.2, in the case of protons, damage to DNA-molecules happens almost exclusively by the proton attracting

electrons away from their molecules, ionizing them. The unbound electrons can then also ionize other DNA-molecules nearby [31]. However, approximately two thirds of radiobiological damage is indirect [32], and most explanations of the FLASH effect have to do with this indirect damage [33]. Usually, three types of DNA damage are distinguished: single-stranded DNA breaks, double-stranded DNA breaks, and base losses [25]. Different molecular biomarkers can detect different types of DNA damage.

2.4.1. Indirect Radiobiological Damage

When water molecules in the cell are ionized, or their electrons become excited, they can hydrolyse to form various reactive oxygen species (ROS). These are molecules that include an oxygen atom with uncoupled electrons, which makes them highly susceptible to reduction reactions. By reacting with DNA molecules, they can damage a DNA base [34]. Because this DNA damage is due to a chemical reaction rather than direct ionization, we speak of indirect radiobiological damage. Cells do have DNA repair pathways for this 'radical DNA damage' [35], as this is a common type of DNA damage. However, hydroxyl radicals (being an example of an alkyl radical, i.e. 'missing' an hydrogen atom, denoted as OH) can react directly with molecular oxygen to form peroxyl radicals [36].

Peroxyl radicals are relatively stable, with a half life of 7 s at 37°C, allowing them to diffuse moderate distances through tissue [37], and can easily abstract hydrogen from molecules with a lower reduction potential. More importantly, cells do not have a repair pathway for peroxyl radical damage. Unlike damage caused by ROS, peroxyl radical damage is not readily chemically repaired [34].

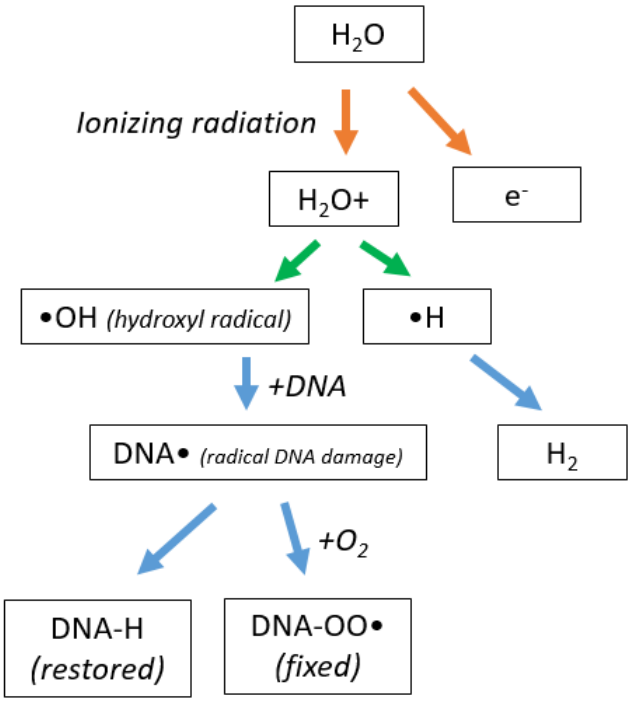

Figure 2.4: Indirect DNA damage by hydroxyl radicals

2.4.2. Dose and Linear Energy Transfer

The amount of radiobiological damage naturally depends on the dose received by the tissue (mostly linearly), but also on the linear energy transfer (LET) of the type of radiation [38]. The LET is the energy deposited per length unit. Note that the LET has the same units as the stopping power, and they are indeed similar quantities, albeit that the electronic stopping power is not the only source of energy deposition. Saying that the amount of damage depends both on dose and on LET might seem a tautology, but they are different quantities (just consider the units: energy/mass versus energy/distance). It is possible to have the same dose deposition with a different LET. In general, the LET provides information about the way a particle interacts with individual molecules, whereas we usually only start speaking

about dose when we describe at least multiple cells, and do not consider individual ionization events at the nano-scale. Also, deeper in the tissue the LET of each particle might be higher, but there might be less particles overall. High LET radiation causes more damage per dose than low LET radiation, because the ionization events are more clustered, overwhelming the cell's repair ability.

It is necessary to consider the radiobiological effectiveness of a type of radiation, when predicting the amount of radiobiological damage a certain dose will do. The LET of a radiation type is usually represented by the radiation weighing factor, a number by which to multiply an absorbed dose to find the equivalent dose, measured in Sievert. Protons are considered high-LET radiation, because as we have seen, the stopping power experienced by the proton is greatest at the end of its path, leading to high LET (which is then also expressed by the depth dose profile, see figure 2.1). Therefore, their weighing factor is 2, as opposed to 1 for photons and electrons. Alpha particles and heavy ions have a weighing factor of 20 [39].

2.5. The Oxygen Depletion Hypothesis

The underlying mechanism of the FLASH-effect is unknown, but it has been hypothesized that the effect is due to oxygen depletion. As outlined in 2.4.1, indirect radiobiological damage caused by free radicals can be repaired in the absence of molecular oxygen, but becomes more potent and irreparable when molecular oxygen is present, due to the formation of peroxyl radicals. Indeed, it is well-established that hypoxic tissue is more radioresistant than normoxic tissue [28].

The mechanism would be as follows: for FLASH radiotherapy, the depletion rate of molecular oxygen due to the formation of peroxyl radicals is higher than the rate at which new oxygen can diffuse into the tissue from the bloodstream. Re-diffusion of oxygen in a single monolayer of cells has been shown to occur within the order of 10^{-2}s [40], which is already similar the duration of an entire FLASH treatment in the order of 10 Gy. While during CONV irradiation the oxygen concentration may only be slightly affected, a local and transient hypoxia might be expected during FLASH irradiation. At some point during irradiation, there will be no molecular oxygen left to form peroxyl radicals, making the tissue more radio-resistant during the remainder of the irradiation.

As this tissue-sparing effect will be less prevalent in tumours (where oxygen concentrations are lower anyway, because they are to a lesser extent oxygenated by the circulatory system), the validity of this hypothesis would provide perspectives towards safer radiotherapy. Figure 2.5 shows how local hypoxic conditions can improve the therapeutic ratio.

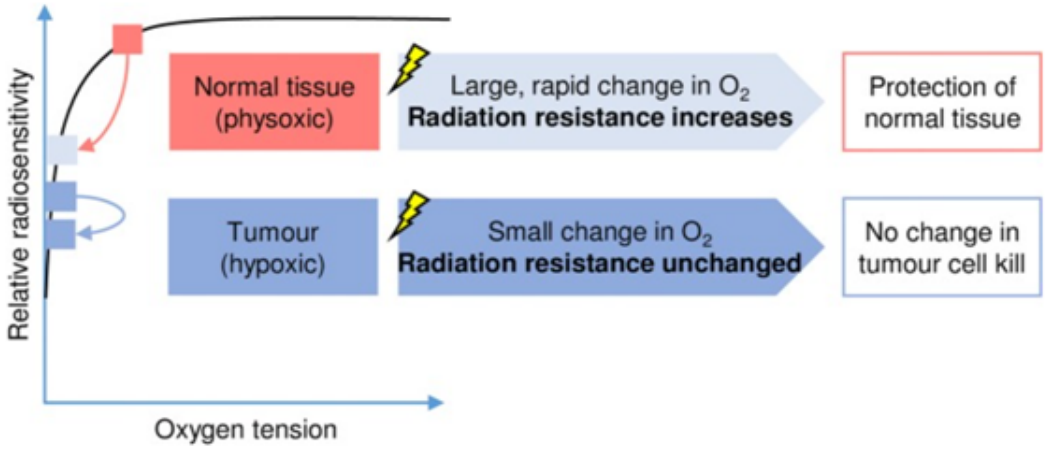

Figure 2.5: Hypoxic conditions tend to increase the therapeutic ratio, because normal tissue becomes more radioresistant while there is little change for the tumour. [28]

2.6. Fluorescence Microscopy

The radiobiological damage at a microscopic level will be investigated using fluorescence microscopy. Instead of capturing the light that is reflected by the sample, or transmitted through it, we capture the light emitted by fluorophores in the sample. The fluorophores are excited by a laser with a wavelength that matches the excitation spectrum of that specific fluorophore. There are multiple ways to attach fluorophores to places of interest, in our case double-stranded DNA breaks. Our method is described in 3.5.

2.6.1. Confocal Microscopy

Confocal microscopy is a particular type of fluorescence microscopy, where only one point of the sample is excited at a time. This way, it is possible to filter the resulting fluorescence from the sample using a pinhole, that does not allow out of focus light to reach the detector. Because almost all of the light will come from around the intended focal plane, confocal microscopes can achieve higher resolutions [41]. There was also a practical reason to choose the particular confocal microscope we used, because unlike other microscopes available to us, the confocal microscope included lasers with emission wavelengths that matched the excitation spectrum of the antibodies we aimed to use.

2.6.2. Co-localisation

Different fluorescent probes excite fluorescence in different wavelengths, which allows for the acquisition of images that consist of multiple color channels, from the same sample. The signals from different channels can be spatially co-localized with each other to better distinguish specific and non-specific signal.

2.7. Monte Carlo Simulations

Monte Carlo simulations numerically model reality using (weighted) random number sampling [42]. They are a very common way to perform particle transport simulations that involve multiple particles, of which the starting positions and momenta can be drawn from a probability distribution. By performing a sufficient number of sufficiently random iterations, by the law of large numbers, Monte Carlo simulations produce an outcome that is the same as if the program had used an entirely different sequence of (pseudo)random numbers. Therefore, for the result to be meaningful, it is not necessary to run the simulation on the same scale as the real-life situation it aims to model. This allows us to drastically remove computation time [43].

It is worth noting that the output of any computer program is, per definition, deterministic. To make sure the random number sampling is pseudorandom, i.e. at least appears uncorrelated, classical computers use huge number sequences where the period after which it repeats is very large.

2.7.1. Particle Interactions in Monte Carlo Simulations

Particle interactions are typically simulated using Monte Carlo methods. In our particle transport simulations, the initial position and momentum of each particle are determined pseudorandomly according to a certain distribution, and then the particles travel in steps through space. At each step particles have a probability of interacting with another particle. Some particles also have a probability of decaying, but in our simulations this will only be the case for secondary particles, as protons do not decay. The program computes the mean free path for protons of the medium it is in, which determines the probability of an interaction. The mean free path (in particle physics also referred to as the attenuation length) associated with particle interactions is given by

$$\lambda = \frac{1}{\rho \sum_i x_i \sigma_i / m_i}, \tag{2.2}$$

where ρ is the density of the medium, x_i the mass fraction of isotope i that causes the interaction we are studying, m_i its mass, and σ_i the cross section of that isotope for that interaction (the cross section can best be seen as a measure for the probability of that interaction happening). Each interaction has its own cross section, which are often determined empirically and tabulated, but also sometimes calculated. The probability of no interaction in a certain path length is then given by

$$P(l) = e^{-\frac{l}{\lambda}}. \tag{2.3}$$

In the case of no particle interaction, the proton just keeps propagating according to its momentum during that step. What happens when the proton does interact, depends on the exact physics settings of the program. Some settings are very elaborate, accommodating almost all possible interactions, others use much simpler models. We use the default physics settings of the Géant4 simulation toolkit (which lies at the source of Topas MC, the environment we use) [44], which covers most particle interactions, including nuclear reactions, scattering, ionization, electron exchange, and excitation [45].

Although interesting, it would go beyond the scope of this thesis to explore the physics settings for each particle interaction. However, as we have seen in Section 2.1.2, the the stopping power, much of the energy deposit, and (consequently) the formation of the Bragg peak, is due to electromagnetic interactions with atomic electrons. Therefore, some brief notes on how simulation toolkits generally handle electromagnetic interactions are useful. Our simulation toolkit, Topas MC, calculates the cross sections for electromagnetic interactions with protons analytically, for each seperate proton, for each step. Direction changes are always neglected. After an electron exchange event with a molecule, or an electron excitation, the excited molecule is not tracked. The energy deposit is just counted at the place of the interaction.

3

Material and Methods

3.1. The Zebrafish Embryo Model

The zebrafish embryo is an immensely popular animal model. The advantages over other animal models (such as mice or cell cultures) in the context of this thesis, are

- Cost-efficiency.
- Rapid embryonic development outside the mother, which makes us able to examine internal organs at a young age.
- Transparency during its larval stages, which allows us to easily examine internal tissue under a microscope.
- Small size, which makes them easy to handle and move between different facilities.
- Being vertebrates, they share many organs which are also present in humans.

In all experiments, we used zebrafish of the ”AB” [46] strain. We had to use a non-genetically modified strain, because the irradiation facility at HollandPTC did not have the sufficient authorisation to conduct experiments with genetically modified organisms. As a consequence, biomarkers that required genetic modifications (like the fluorescent labelling of certain cells) were not available for this project.

3.2. Zebrafish Embryo Handling

3.2.1. Breeding

The embryos were obtained by crossing adult zebrafish, which are maintained at 28°C on a 14:10 light cycle. Pairs were put together in a tank overnight in a double-bottomed tank, such that the eggs can fall through. The fertilised eggs were sieved the following morning or early in the afternoon, after which we rinsed them in egg water (60 μg/ml sea salt in distilled water [47]) and transferred them from the sieve into several petri dishes filled with egg water ($\varnothing$10cm), such that each dish would contain 50-100 embryos. The embryos were then stored in a 28°C incubator until the next stage of the experiment. Live embryos were always kept in egg water, never regular water. Embryos were also never kept longer than 5 days post fertilisation (dpf), to adhere to the EU Animal Protection Directive (2010/63/EU) and the TU Delft Animal Welfare Committee, which have stricter guidelines for later life stage zebrafish.

3.2.2. Transfer to HollandPTC

Because acute hypoxia is required at the time of irradiation, and we found that the oxygen saturation of the water would rise rather rapidly after stopping oxygen regulation 4, we were allowed to conduct the next stages at HollandPTC’s bio-lab (considering the time between mounting and irradiation already tended to take more than an hour, even without transportation).

The morning of an irradiation day, we would transfer the embryos to 50ml falcon tubes using 7,5ml VWR disposable transfer pipettes. This happened when the embryos would be 3 or 4 dpf. Older

ages were not possible, because we could only euthanize and further process the embryos a day after irradiation (irradiation could take until very late at night, and after irradiation the water and well plate would also remain activated for a few hours, making it impossible to take them out of the radiation facility), and we could not exceed 5dpf due to animal welfare regulations. Also, we did not want to euthanize and dehydrate the embryos directly after irradiation, to allow effects of the radiobiological damage to become apparent. We also did not want to use earlier ages, because there wouldn't be as many distinguishable organs to investigate and notice possible organ-specific effects.
We would put the falcon tubes in a styrofoam box, use paper towels and tape to fix them to the bottom of the box to minimize bustle, which would exhaust the fish, and move them by bike.

3.2.3. Before Irradiation

Before irradiation, the embryos were transferred either to a petri dish with normal egg water (as a control) or to the hypoxic aquarium to receive hypoxic treatment 3.3.2. We would then transfer them by pipette to Thermo Scientific flat-bottom 96-well microplates (in some CONV experiments, a 24-well plate was used, but for FLASH experiments we switched to smaller wells to guarantee sufficient field homogeneity), to be mounted in the irradiation setup (Section 3.4). The hypoxic treatment caused significant mortality, so to avoid irradiating embryos that were already dead, we checked their heartbeats under a simple optical transmission microscope. Immobility was not a reliable indication of death, as many live embryos would also be immobile in the hypoxic condition.

3.2.4. After Irradiation

After irradiation, we transferred all embryos to petri dishes with normoxic water and in the (windowless, therefore dark) incubator at HollandPTC 28°C to stay overnight. The next day, they were picked up between 1 and 4 pm (depending on the availability of the radiation technician) and transferred back to the incubator at the Applied Sciences building, again using falcon tubes and a styrofoam box. There they stayed in the 28°C incubator until further processing.

At the desired time, embryos were euthanized for further analysis. Euthanasia was achieved by transferring the embryos from their petri dishes to falcon or Eppendorf tubes, and putting them in ice for 1 hour or more. After this, they were dehydrated by putting them in 25% methanol for 5 minutes, then 50% for 5 more minutes, then 75%, and then stored in 100% methanol in the freezer for further processing. Spare embryos reaching the age of 5dpf were also euthanized and then discarded in the freezer as animal waste.

3.3. The Hypoxia Chamber

The design from the hypoxia chamber was adapted from [48]. The embryos stayed in an aquarium which contained a dissolved oxygen measure-and-control unit, which could decrease the dissolved oxygen concentration by dispersing nitrogen into the water, to drive out and replace the oxygen. The water was stirred to make sure the oxygen pressure was homogeneous throughout the aquarium.

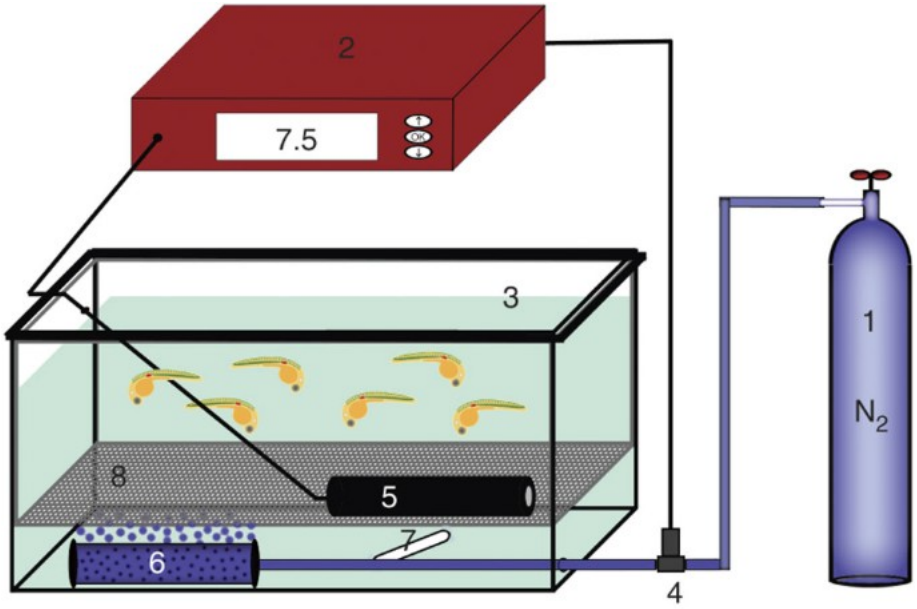

Figure 3.1: Hypoxic Aquarium Setup [48]. 1. ≥99,9% Pure pressurized nitrogen. 2. Oxygen regulator. 3. 1L Sealed aquarium. 4. Solenoid valve. 5. Galvanic oxygen probe. 6. Air stone. 7. Magnetic stirrer. 8. <200 Micron mesh.

Rather than buying a commercial oxygen regulator setup, we custom-built our own. The gas control set which included the air stone, tubing and Burkert solenoid valve, was supplied by Loligo Systems (catalogue #AC10050). The control unit was the programmable LED indicator PR5714 (with relays and analogue output) by PR Electronics. The dissolved oxygen probe was the Oxyguard Mini Probe (catalogue number D161SV).

3.3.1. Calibration

The oxygen meter was calibrated by putting the probe in freshly poured egg water, without magnet stirrer, with the lid on (which is not airtight). This is considered the 'normoxic' state, and defined as 100% aeration. In the fish lab environment where the hypoxic aquarium was placed, this corresponded to a voltage output of 13.71 mV. The oxygen probe has a true zero and linear output, so no sensor output was defined as 0% oxygen saturation.

3.3.2. Hypoxic Treatment

The initial hypoxic treatment consisted of incubating the embryos at 8% saturation for 6 hours. This was later improved, to 10% saturation for 120 minutes in the final experiment. The fine-tuning of the hypoxic treatment is elaborated upon in chapter 4.

3.3.3. Accuracy

The PR5714 has an accuracy $\leq \pm 20$ μV, which translates to $\leq \pm 0.146$ % (as one percentage point corresponds to 137.1 μV). The Oxyguard Mini has an accuracy of 1% within the measured voltage. Importantly, the PR5714 has a minimal measurement range of 0-1V and a 4-digit display readout, which means we can only read out full percentage points. If we consider the case where the oxygen saturation is 50%, the PR5714 could be 0.146 percentage point off, the Oxyguard Mini as much as 0.5 percentage points. Also considering the resolution of 1 percentage point, a display readout of 50% could indicate an actual value as low as 48.85% or as high as 51.15%. Similarly, the uncertainty due to the instrumentation in a display readout of 8% would be ± 0.726%.

We did consider increasing the resolution by transforming the detector output before giving it as input to the control unit, but ultimately decided the current accuracy was sufficient and this would not be worth the cost. Furthermore, it would make little difference for the control unit, as it cannot control the dissolved oxygen concentration accurately beyond one percentage point anyway.

3.4. The Irradiation Setup

3.4.1. The Low Dose Rate (CONV) Setup

Figure 3.2 shows the passive scattering setup used at the HollandPTC proton radiation facility, that was used for the CONV experiments. The setup was designed, realised and by HollandPTC's radiation technicians, and optimised before each radiation session. This section explains the working principles and the elements that were used. The image is adapted from [26].

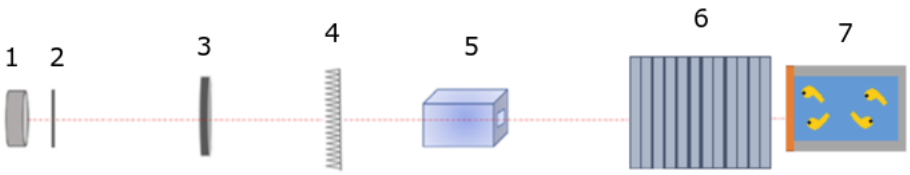

Figure 3.2: CONV irradiation setup. 1. Beam exit window. 2. Lead scatter foil. 3. Dual ring scatterer. 4. Ridge filter. 5. Collimator. 6. Water Equivalent Thickness slabs. 7. Well with samples.

The beam leaves the cyclotron with a Gaussian shape, with higher intensity in the middle than at the edges. To convert this to a beam with a homogeneous profile in the lateral direction, to guarantee the same dose deposition throughout the sample, the beam needs to be scattered. In the setup optimised for a 150 MeV mono-energetic exit beam, this was achieved by first having the beam traverse a single lead scattering foil, and then a dual scattering ring. A scattering ring scatters protons hitting the centre most, and those at the edges least, which is useful if you need to change the lateral beam profile from Gaussian to flat, like for our experiment. In our case, the centre of the ring was lead, the edges were aluminium. With a flat profile, the beam reaches the ridge filter produced by GSI Darmstadt [49], which modulates the energy spectrum to produce the SOBP in water (as explained in chapter 2). Before reaching the sample, the beam is collimated using a squared aperture, such that the beam reaching the sample has a 'clean' square and flat lateral profile. The collimator consists of a 25cm long PMMA (a low-Z material) part, and a 70cm brass (high-Z) part.

As we want the well which contains the embryos to be situated at the plateau of the SOBP, there needs to be a volume of water before the well. This is because the plateau only begins at a certain penetration depth (as shown in figure 2.2). To achieve this, we use a row of water equivalent thickness (WET) slabs (which can conveniently be made longer or shorter by adding or removing slabs, as opposed to an actual water tank), such that when the beam reaches the embryo well, it will be at the SOBP. The well itself is part of a ThermoFisher 96-well flat-bottom polystyrene well plate, mounted vertically, filled with water to the brim, and capped with a 3D-print resin cap (custom made). A single well could hold up to 50 embryos, and if there were enough embryos available we would try to reach that limit to have a sample size as large as possible. The well plate is also modelled in the simulation, so Section 3.8.4 elaborates further on the wells. Figure 3.3 shows what the well plate looks like in reality.

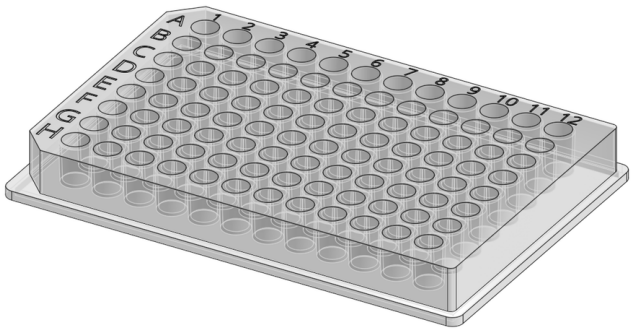

Figure 3.3: A rendering of the flat bottom (F-bottom) standard type 96 well plate [50]

3.4.2. The High Dose Rate (FLASH) Setup

The FLASH setup is slightly different, because we could not allow as much passive scattering, to not lose to much of our dose rate. For FLASH, there is a trade-off between dose rate and field size, which was not at play in the CONV setup because the dose rate did not have to be high. If anything, it should be low to contrast FLASH irradiation.

Simulations confirmed we could not achieve sufficient homogeneity by applying the maximal possible dose rate (which would amount to just using the unscattered pencil beam) and using the same setup as for CONV irradiation (these results are displayed in Section 4.5.4). Ultimately, we had the choice to use the unscattered pencil beam and only use a very small field size, or to still use only the single scatter foil and have a slightly larger field size, but a lower maximal dose rate. Based on single measurements on the lateral beam profile for both cases [51], the properties of the two possible setups were as shown in Table 3.1.

Setup	Without Scattering Foil	With Scattering Foil
Field diameter	2mm	15mm
Nominal field homogeneity	99%	97%
Maximal dose rate	200 Gy/s	40 Gy/s

Table 3.1: Properties of the FLASH setup with and without scattering foil.

Between these options, we decided to choose the setup that still included the scattering foil, because it would prove very impractical to immobilise the embryos in a 2mm diameter field. The fish would have to be completely immobilised, which would require an entirely different setup, or filling the wells with agarose instead of water. Previous experiments where the embryos were fixed in agarose, concluded that this should not be done if it could also be avoided [52]. Also, we were expecting high mortality and could not risk the embedding in and removal from agarose to be another chance at losing surviving embryos. It would also be very time-consuming, leading some embryos to spend much longer in the agarose than others, adding another variable to the experiment. Meanwhile, a field diameter of 1.5cm would allow us to remain using the 96-well plates (where the well diameter is 0.5cm), filled with water, and having the embryos swim around freely. Also, a dose rate of 40 Gy/s is sufficient and still qualifies as FLASH. Consequently, the FLASH setup only contained the elements described in figure 3.4

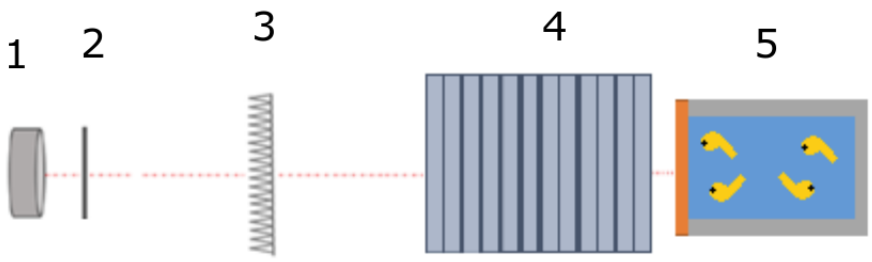

Figure 3.4: CONV irradiation setup. 1. Beam exit window. 2. Lead scatter foil. 3. Ridge filter. 4. Water Equivalent Thickness slabs. 5. Well with samples.

3.5. Immunohistochemistry Staining

To assess the radiobiological damage in the embryos that were stored in the freezer after their treatments, we stained them with the γ-H2AX antibody. γ-H2AX binds to double-stranded DNA breaks, so the prevalence of γ-H2AX in the sample will then be a measure for the radiobiological damage it has suffered. γ-H2AX does not excite fluorescence itself, so we also needed a second antibody that is fluorescent and binds to γ-H2AX. Ultimately, it is the amount of fluorescence from the secondary antibody that is the data we actually could collect using the confocal microscope. Consequently, we might also refer to γ-H2AX as the primary antibody.

The secondary antibody that we used is Alexa Fluor® 488 (ab150077). All commercially available antibodies are derived from animals, and our primary antibody was generated in rabbits. The kind of secondary antibody that specifically binds to rabbit antibodies are 'anti-rabbit' antibodies, which can be obtained by immunizing a non-rabbit (usually a goat) by injecting it with rabbit Immunoglobulin-G (IgG, another antibody). Alexa Fluor® 488 is generated in goats and therefore a 'Goat Anti-Rabbit' antibody, meaning it is an eligible secondary to a rabbit-generated primary [53].

The antibody staining requires a series of steps in which the embryos need to be immersed in different solutions. Practically, we conducted these steps by keeping the embryos (up to 10 together) in a 24 well plate insert with a mesh bottom, such that they could easily be transferred from one well to another. The wells could then be prepared in advance to contain the desired solutions (in the case of our 24 well plates, each well contains 1.5 ml). This allowed quick and convenient transfer of the embryos from one solution to the next.

3.5.1. Primary Antibody Binding

First, the embryos were re-hydrated from being stored in a methanol solution. To this end they were immersed in a 75% methanol solution for 5 minutes, and then likewise in 50% and 25%. The remaining part of the solution consisted of Phosphate Buffered Saline (137 mM NaCl, 2.7 mM KCl, 10 mM Na_2HPO_4, 1.8 mM KH_2PO_4) (PBS), which is meant to be isotonic with zebrafish cells, meaning it has similar osmolarity and ion concentrations, as not to damage them with osmotic shock. They were then washed (3x5 minutes) in PBS with Tween™20 (PBS-Tween), a detergent that reduces non-specific antibody binding and protein-protein interactions [54].

We then transferred the embryos to a 100 mg/ml collagenase solution. The collagenase is meant to digest some of the embryo's outer membrane to make the body more permeable by the antibodies. Initially, this digestion step took 30 minutes, but in later experiments we increased this step to 60 minutes as we were not satisfied by the amount of antibody penetration. Even though were hesitant to increase the digestion time too much, as to not damage the embryos or make them too vulnerable during pipetting, we did not experience that embryos required more delicate handling after 30 minutes longer digestion. The collagenase was then washed off in three more washes with PBS-Tween, 5 minutes each.

The next step was to immerse the samples in a solution containing another blocking agent, goat serum. The aim of the goat serum was to block non-specific binding of the secondary antibody, which is goat-generated. The serum especially blocks so-called Fc receptors, proteins that are found on cell surfaces [55]. The blocking solution consisted of 10% goat serum diluted in PBS-Tween. Embryos remained in the blocking solution for 60 minutes.

Hereafter, we transferred the embryos to a fresh blocking solution (of the same ingredients). To this solution, we finally added our primary antibody, the γ-H2AX (7.5 μl antibody per 1.5 ml well). The immersed embryos were then transported on ice in a styrofoam box to the cold room (4°C) in another building. There, they were placed upon a rocking table at 40 rpm to incubate overnight. The primary antibody would then have the chance to bind to double-stranded DNA-breaks.

3.5.2. Secondary Antibody Binding

The morning following the overnight incubation of the primary antibody, the embryos were brought back from the cold room. The blocking solution with the primary antibody was washed off in PBS-Tween (4x 15 minutes). Before incubation in the secondary antibody, the well plate containing the solutions was wrapped in aluminum foil, to keep the samples and the solutions in the dark, as not to photo-bleach the fluorophores of the secondary antibody. From now on, the embryos would be kept in the dark until after they had been imaged. The samples were then incubated for two hours in the goat serum blocking solution, with 3μl secondary antibody added per 1.5 ml well, at room temperature, on the rocking table. After the incubation, the samples were washed again in PBS-Tween (2x 20 minutes).

3.5.3. DAPI Staining

Lastly, the samples were incubated 2 hours in a DAPI working solution (1μg/ml DAPI in PBS-Tween). DAPI is a fluorescent stain that binds to chromatin, allowing us to excite fluorescence in the cell nuclei. This knowledge helps us avoid interpreting signal as being caused by a double-stranded DNA break, while in fact there is no DNA at that location. After the DAPI incubation, they were washed in PBS-Tween (2x 20 minutes) and then in PBS (4x 5 minutes). From the PBS, they could be mounted right away, or stored in the fridge at 4°C.

3.6. Mounting and Imaging

To mount the stained samples in the microscope, we would transfer them from the PBS in which they were stored to liquid glycerol. From the PBS we transferred them to a 75% PBS and 25% glycerol solution for 20 minutes, then 50%, and then mounted on a glass slide in a drop of 75% glycerol. We then took a cover glass with small pieces of gum attached to the corners such that there would remain a 1-2mm space between the slide and the cover glass, as to not squish the embryos, which were very delicate. We would then close off the edges of the space between the slide and cover glass with nail polish. Embryos were mounted on the side as this was the most stable position, minimizing the possibility that they would be damaged in an effort to reorient them, while still having a largely consistent orientation over all the samples. Moreover, all of above steps had to happen in the dark, to not photo-bleach the antibody stains.

Mounted embryos were transferred to the confocal microscope (which was in another building in a styrofoam container filled with ice, and remain there while the other samples were being imaged until they were brought back to the 4°C fridge in the lab.

We used the commercial Nikon confocal microscope to capture the fluorescence by the DAPI stain, which has an excitation peak around 358nm, and the γ-H2AX labeled with Alexa Fluor® 488 (which, of course, excites fluorescence at 488nm). This requires two different lasers, as the excitation spectra have almost no overlap. This is no coincidence, as we did not want to have fluorescence from one channel 'leak' into the other. For each embryo we captured images of focal planes over the whole range of visible specific signal, with 1.5-1.75 μm between planes. Top, bottom and step size had to be entered manually for each sample, after which the rest of the image acquisition was automatic. Both channels were captured simultaneously but stored separately. Depending on the embryo, this produced a Z-stack of 60-80 focal planes over 100-120 μm, which could then be max-projected or investigated separately to provide 3D information about the embryo. We could also co-localize the Alexa Fluor® 488 and DAPI channel.

3.7. Colocalization

This section provides a step-by-step description of the colocalization protocol, once the images are obtained.

3.7.1. Step 1: Find a Piece of Muscle Tissue in the MAX-Projection

Across all samples, the muscle tissue along the spine generally turned out to have the most consistent specific signal in the γ-H2AX channel. To make a meaningful comparison between samples, we need to compare the same piece of tissue, and this piece of muscle tissue is the best candidate. Other pieces of tissue which tend to have a lot of specific signal, like the heart, are not consistently visible in all images.

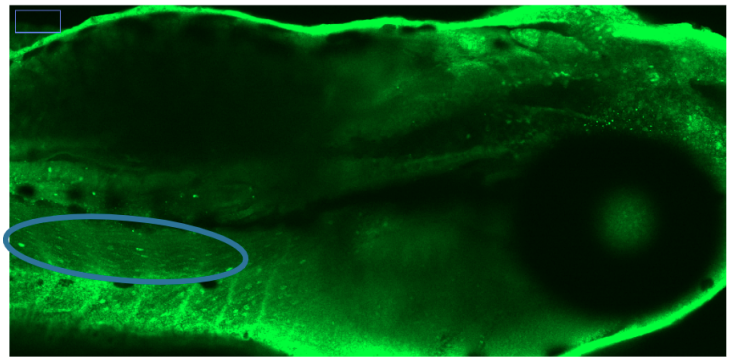

Figure 3.5: Finding a piece of muscle tissue

3.7.2. Step 2: Select the Relevant Slices and Region of Interest

After a satisfactory portion of the image is selected in the MAX-projection, we manually find the focal planes where the signal is from, and remove all focal planes and regions that are not relevant.

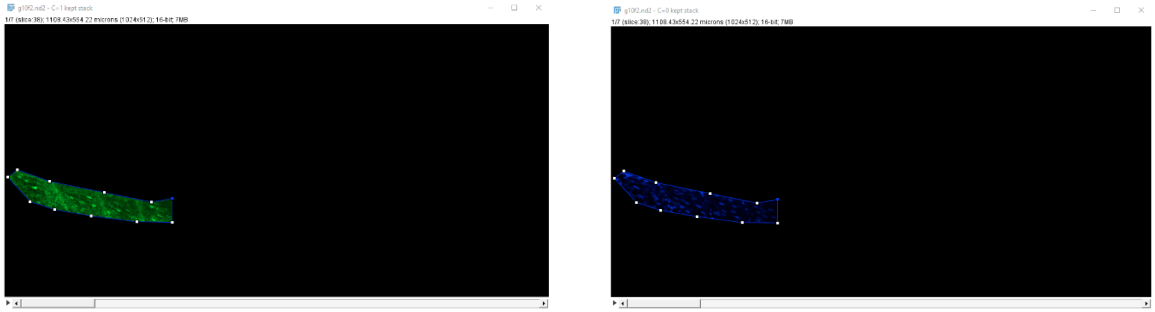

(a) γ-H2AX **(b)** DAPI

Figure 3.6: Selected focal planes and ROI in the γ-H2AX channel, and the corresponding portion of the DAPI channel.

Figure 3.7 provides a zoomed-in and enhanced (by optimizing brightness and contrast) MAX-projection of the selected portion of the sample considered here.

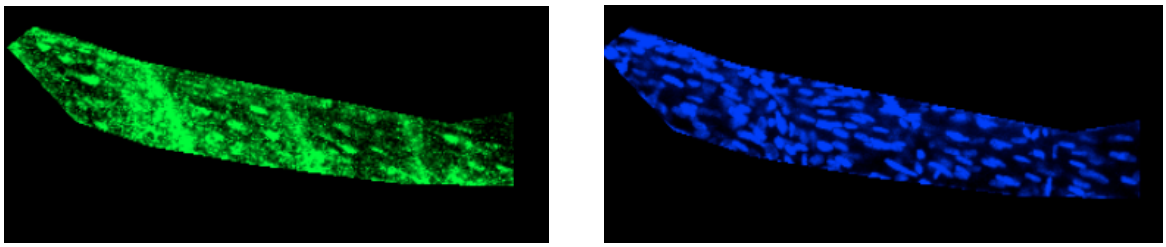

(a) γ-H2AX, enhanced **(b)** DAPI, enhanced

Figure 3.7: MAX-projections of the selected portion from the sample in figure 3.5, brightness and contrast optimized.

3.7.3. Step 3: Apply a Threshold to the Selected Portion

Next, we apply a threshold to the image, keeping the signal with an intensity above the threshold and removing the signal below. The value of the threshold was chosen manually, to guarantee an appropriate value for each sample.

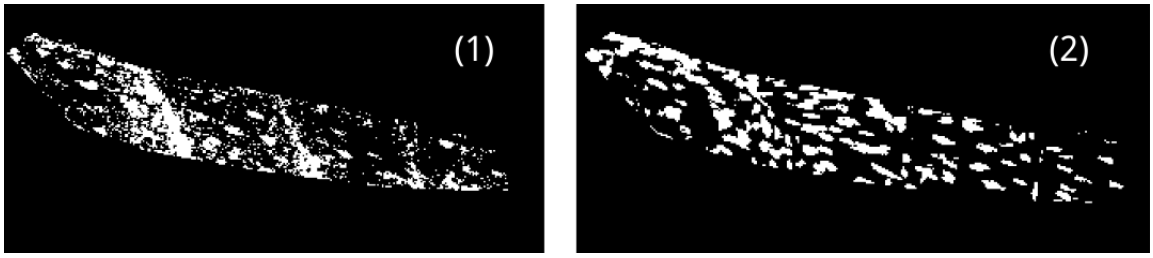

Figure 3.8: Thresholded images. (1) γ-H2AX. (2) DAPI.

3.7.4. Step 4: Merge the γ-H2AX and DAPI channels

To further remove non-specific signal in the γ-H2AX channel, we only want to keep signal at places where we know there is DNA present, based on the DAPI channel. To this end, we merge the channels, and see where they overlap. We then keep the signal where the γ-H2AX coincides with the DAPI channel.

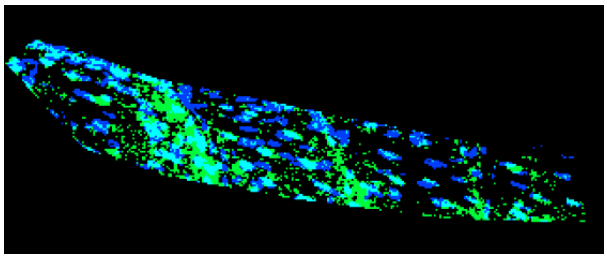

Figure 3.9: The selected γ-H2AX and DAPI signal merged, overlap highlighted. Green: γ-H2AX. Blue: DAPI. Cyan: overlap.

3.7.5. Step 5: Find the area fraction of the γ-H2AX signal

We have reduced the γ-H2AX signal to only contain a relevant selection of focal planes, a relevant region, a sufficiently high intensity, and only signal that coincides with the loci of actual DNA. The final step is to find out how large the area is that we are left with, compared to the area of all DNA present. Our final endpoint is the area fraction of the specific γ-H2AX signal (which should represent the amount of double-stranded DNA breaks), and the area of the DAPI signal (which should represent the total amount of DNA in the selected portion).

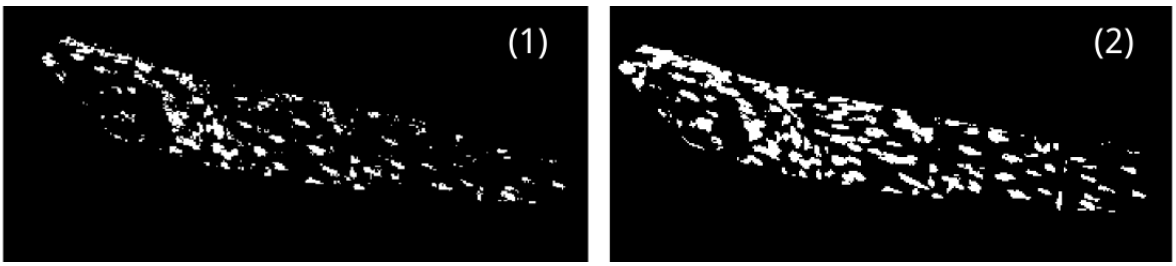

Figure 3.10: The endpoint of our colocalization is the fraction of the white area in (1) of the white area in (2). (1) The overlap region from figure 3.9. (2) The DAPI region from figure 3.8.

3.7.6. Summary

Figure 3.11 provides a summary of how we extracted specific signal from a Z-stack portion.

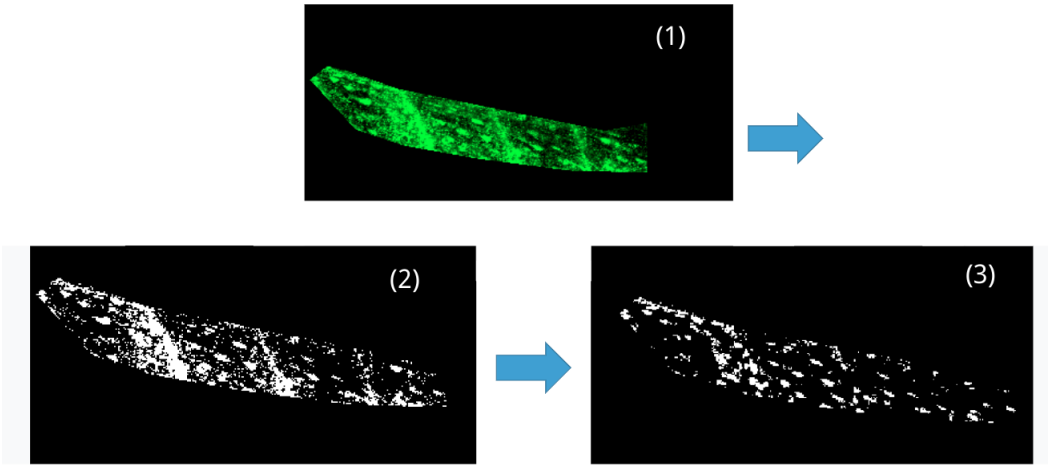

Figure 3.11: Extracting specific signal from an image. (1) MAX-projection of the selected focal planes and ROI. (2) Threshold applied. (3) Co-localized with DAPI channel.

3.8. Topas Monte Carlo Model

3.8.1. Physics Settings

In the simulation, we used Topas MC's default physics settings. These were considered sufficient as we were not investigating any specific or rare interaction, or an unusual energy range. The default Geant4 physics list that TopasMC will use contains the modules listed in Table 3.2 [56]:

Modules	Content
g4em-standard_opt4	Electromagnetic interactions
g4h-phy_QGSP_BIC_HP	Nuclear interactions
g4decay	Decay of excited residual nuclei
g4ion-binarycascade	Nuclear interactions of light ions
g4h-elastic_HP	Elastic scattering
g4stopping	Capture of charged particles at rest

Table 3.2: TopasMC's default physics modules, as used in our simulation.

3.8.2. The Beam Model

Beam Characteristics

The beam of our CONV setup were characterized previously [26]. In the future, the FLASH beam will be characterized separately, but as we were conducting the first FLASH experiments, this had not happened at the time of our experiments. The beam characteristics were first fine-tuned for a 150 MeV proton beam ([26], Table 4.10). However, the same values for the angular spread also described the beam *after* traversing the passive scattering setup, i.e. after many protons had scattered and the beam energy at the target had dropped to 116.1 MeV ([26], Table 4.11). Furthermore, differences in position- and angular spread between different proton energies were considered negligible when simulating the energy spreading of the ridge filter [23]. Because these characteristics are applicable to the beam with and without passive scattering, regardless of the energy, we decided that these beam characteristics could also reasonably be used to model a FLASH beam profile from the same particle source. The difference between the FLASH and CONV beam profiles lies in the position distribution, the shape and size of the field, and energy spread. We simulate two setups for the FLASH beam, one where we use the bare pencil beam and one where we model the half-scattered pencil beam described in Section 3.4. All beam characteristics for each simulation can be found in Table 3.3.

Beam Characteristic	Value CONV	Value FLASH bare beam	Value FLASH half-scattered
Position Distribuition	Flat	Gaussian	Gaussian
Position cut-off shape	Rectangle	Ellipse	Ellipse
Position spread (x)	-	0.27 cm	2.96 cm
Position spread (y)	-	0.21 cm	2.96 cm
Postion cut-off (x)	1.35 cm	7 cm	2 cm*
Position cut-off (y)	1.35 cm	7 cm	2 cm*
Angular distribution	Gaussian	Gaussian	Gaussian
Angular spread (x)	0.0027 rad	0.0027 rad	0.0027 rad
Angular spread (y)	0.0032 rad	0.0032 rad	0.0032 rad
Angular cut-off (x)	90	90	90
Angular cut-off (y)	90	90	90
Energy Spread	0.94	0.8	0.8

*We would have preferred to use a larger position cut-off here, similar to the one used for the bare beam. However, because the half-scattered beam is much more spread out compared to the bare beam, this would require a larger simulation to have the same amount of protons hit the area of interest.

Table 3.3: The beam characteristics used for each simulation.

Energy Spectrum

The energy spreading effect of our ridge filter has also been investigated, both experimentally [26] and computationally [23]. To obtain a realistic energy spectrum, there are two options:

- Define an SOBP, such that it had the same modulation width as the experimentally found SOBP produced by our ridge filter. We then reverse-engineered the energy spectrum that would produce that SOBP in water. This was the approach taken previously by [52].
- Look at simulations of our specific ridge filter to predict the energy spectrum.

The first option has the advantage that the result is directly derived from actual experimental data, but the downside is that any particular artifacts of our specific ridge filter are lost. It will just produce a 'generic' energy spectrum, that only has the modulation width of its SOBP in common with the actual energy spectrum.

The second option gives more information about our particular setup, but the energy spectrum will only be based on the computational model. A further disadvantage is that the ridge filter simulations did not include the passive scattering setup. As a consequence, we cannot directly use the energy spectrum from the ridge filter simulation as input for our CONV simulations. We need to assume the energy spreading effect of the filter is the same for 116 MeV (the energy at the ridge filter in the CONV setup), as it is for 150 MeV (the energy previously used in the simulation without the passive scattering elements [23]). Ultimately, the second option was implemented into the model, a departure from [52]. This means we adapted the energy profile after the ridge filter from [23], but with all energies shifted by 32.4 MeV such that the peak is at 116 MeV. Figure 3.12 shows the energy spectrum of the input beam. Even tough the data entry consists of discrete values and weights, TopasMC will interpolate and use a continuous energy spectrum for the simulation, as the 'BeamEnergySpectrumType' is set to 'Continuous'.

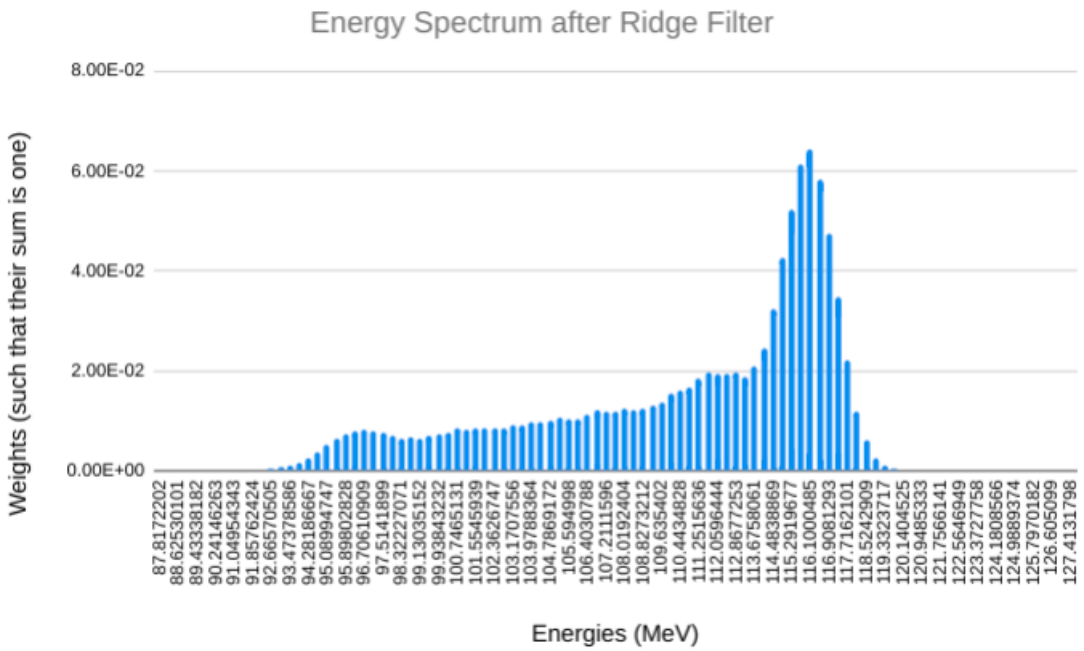

Figure 3.12: The energy spectrum of the input beam

3.8.3. Geometry Overview

Now that we know how to reasonably model the beam, with the characteristics it has *after* the collimators and the passive scattering setup (in the CONV case), we do not need to simulate the entire setup again. Our computational model only includes water to simulate the water equivalent slabs, and the well plate itself. The beam that enters the model on the left side is meant to represent the beam as it leaves the collimator. Figure 3.13 gives an overview of the elements present in the model. All dimensions correspond to those in reality. More details about the geometric and material makeup of the model can be found in the model description in appendix A.

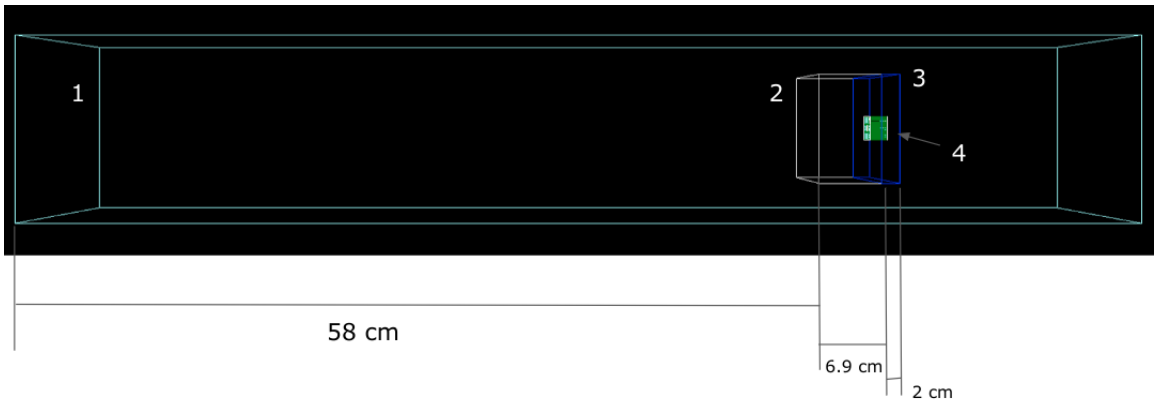

Figure 3.13: Overview of the Topas Monte Carlo model in the Topas graphical interface 1. Boundaries of the simulation 'world'. The beam enters from the left, as it were leaving the collimator. 2. WET slabs, modelled with Geant4 water. 3. Well plate, modeled as a mixture of air and polystyrene 4. Centre of the well plate which is modelled in more detail.

3.8.4. The Well Plate Model

Instead of separately simulating all 96 wells from the 96-well plate, we simulated the well plate as a homogeneous mixture of air and polystyrene, except for the target well and the 8 wells surrounding it, which were actually individually simulated in a 3x3 grid. The middle well was filled with water, whereas the rest remained filled with air. In reality only the wells that contained fish were filled, and they were never adjacent so that one well would not get irradiated during another well's irradiation. The well

plate was sealed with a 1 mm epoxy-resin cap, modelled as a slab of carbon, hydrogen and oxygen (fractions 0.35/0.53/0.12), covering the entire well plate. Figure 3.14 shows the centre of the well plate in the TopasMC model.

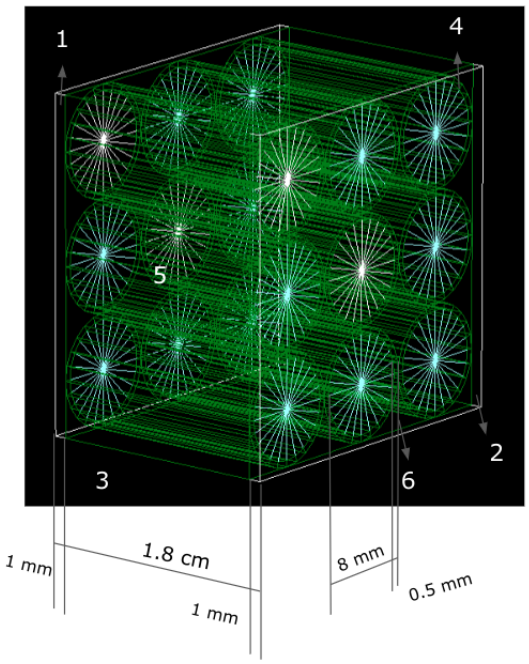

Figure 3.14: Close-up of the well plate centre in the Topas graphical interface 1. 3D-print epoxy resin lid. 2. Polystyrene bottom 3. The exterior, modeled in less detail as a homogeneous mixture of air and polystyrene. 4. Polystyrene edge of the well. 5. Inside of the well, filled either with air or water. 6. Space between the wells, filled with air.

3.8.5. Scoring

We defined a box-shaped scoring volume around the middle well which was divided into 'voxels', little volumes that count the dose they receive. The scoring volume was divided in 25 bins in the x-direction, 25 bins in the y-direction, and 4 bins in the z-direction. Figure 3.15 shows schematically how the well is divided, and a rendering of the model in its TOPAS graphical environment.

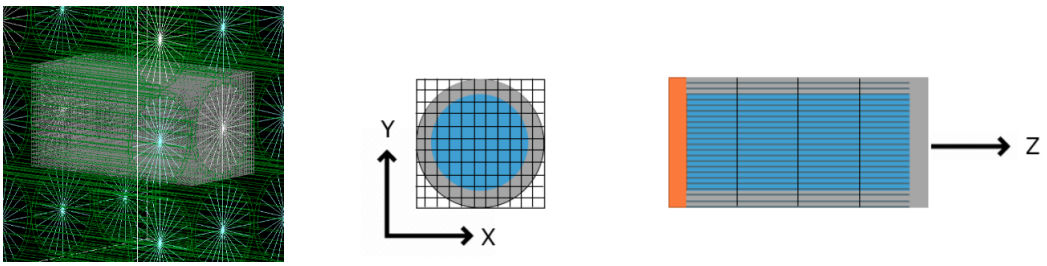

Figure 3.15: The scoring volume is box-shaped and divided into 25x25x4 voxels. In each voxel we tally the received dose. The amount of voxels portrayed in the schematic is not the actual amount.

3.8.6. Simulation to Validate the Energy Spectrum

Before running the actual simulations, we validated the energy spectrum, to see if it would indeed produce the desired SOBP. The scoring volume in the water, through the well plate, is a 11cm cylinder with its base perpendicular to the beam. The cylinder is binned along the direction of the beam, in 200 bins. Unlike the scoring volume for the actual calculations described in Subsection 3.8.5, it is not binned in the lateral direction, because we are only interested in the beams behaviour along the propagation direction. Consequently, the value scored is the energy deposited in the entire cylinder-slice. A rendering of the scoring volume in the TopasMC environment is depicted in Figure 3.16. Different radii for the cylinder were used, to see how the size of an object's projection in the direction of the beam

influences the result (e.g. due to artifacts of the simulation).

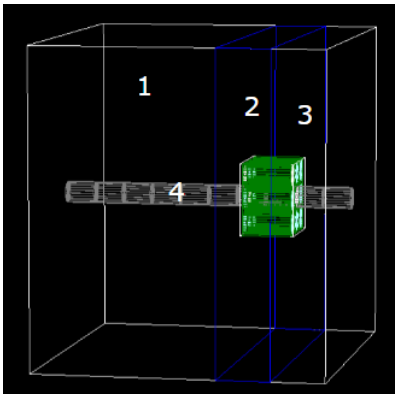

Figure 3.16: The scoring volume in the energy spectrum validation simulation. 1. Body of water. 2. Well plate. 3. Extra volume of water after well plate, to also capture the tail of the SOBP. 4. Cylindrical scoring volume.

3.9. Homogeneity Calculations

After running the simulation, the homogeneity of the dose in a certain region of interest is defined by the maximum dose to any discrete volume in that region (D_{max}), and the minimum dose (D_{min}), in the following way:

$$H[\%] = 100 \left(1 - \frac{D_{\text{max}} - D_{\text{min}}}{D_{\text{max}} + D_{\text{min}}}\right). \tag{3.1}$$

The dose uniformity will be an important metric in judging the quality of the irradiation setup.

4

Results and Discussion

4.1. Re-Oxygenation of Hypoxic Water

A few short experiments were done to determine how long water would stay hypoxic under various circumstances. To this end, we brought the water to an hypoxic state, and then turned off the nitrogen supply. In some cases, we made an effort to minimize diffusion of oxygen from outside the aquarium by sealing all holes and the edges of the lid with duct tape. It should be noted that this did not make the aquarium completely airtight and there still remained air inside the aquarium (we did not change the water level, which remained halfway before the edge of the aquarium). The water was either gently stirred, left unmoved, or the oxygen probe was gently replaced after each measurement. The results are plotted in figure 4.1.

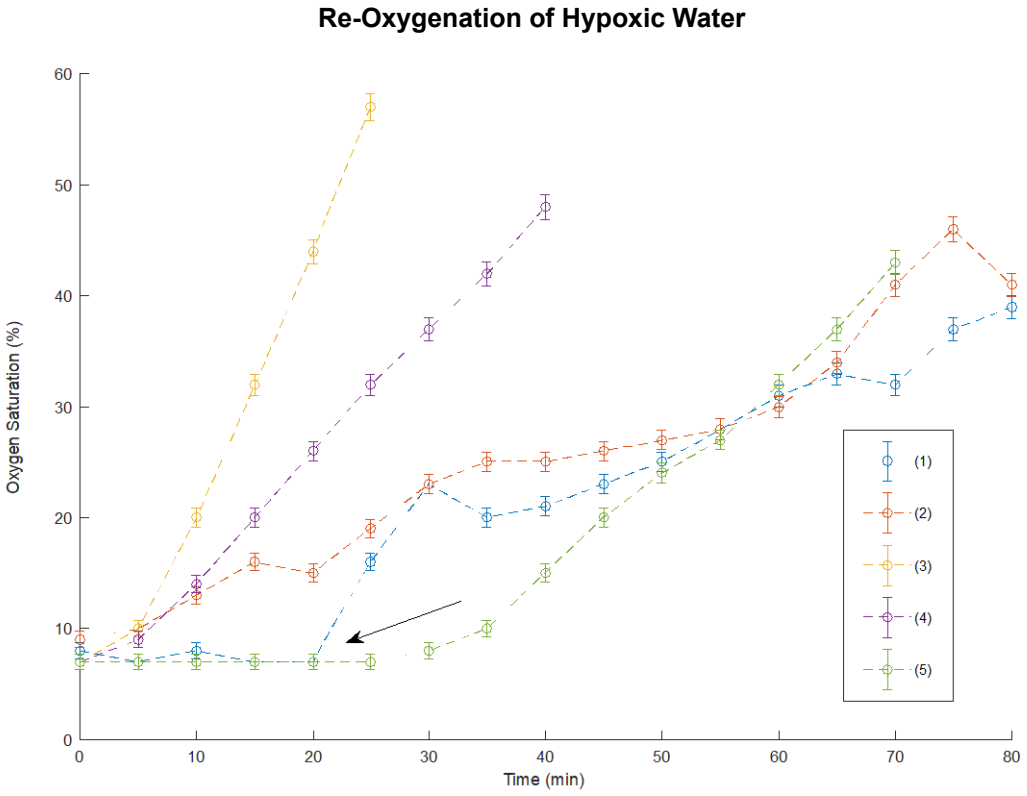

Figure 4.1: Re-oxygenagion after hypoxia. 1. Unsealed, gentle probe replacement after arrow. 2. Sealed, gentle probe replacement throughout the experiment. 3. Unsealed, stirred. 4. Sealed, stirred. 5. Unsealed, unstirred, no probe replacement.

First, we see that without stirring it does not seem to make a big difference whether an effort was made to seal the aquarium or not. This means the air inside the aquarium contained a high enough oxygen pressure to re-oxygenate the water, at least until 30% saturation. With stirring, we see that the prevention of new oxygen diffusing into the aquarium does make a difference.

Second, we see that without stirring or gently replacing the oxygen probe, the dissolved oxygen concentration seems to remain very low for 30 minutes. However, we suspect this result to be misleading: in experiment (1) where the probe is left unmoved for the first 20 minutes and then gently replaced afterwards, the measurement value immediately increased a lot by the next measurement. The suspiciously low measurement values might be explained by the fact galvanic oxygen probes dissipate a small amount of oxygen themselves (because they use an oxygen reduction reaction to produce current), and therefore create a low dissolved oxygen concentration locally. This underlines the importance of stirring the water during oxygen regulation.

Because of these results, we did not trust the fish to remain acutely hypoxic during transportation and irradiation. We therefore decided to take the entire hypoxia chamber, including nitrogen supply, to HollandPTC. This way, we could guarantee acute hypoxia until right before irradiation.

4.2. Embryos in Hypoxia

Even though Zebrafish embryos breathe by diffusion through the skin [57], it cannot be assumed that the embryo tissue has the same oxygen pressure as the water it stays in. However, it was clear that being in hypoxic water does physically affect the embryos because they all stop swimming around within the first hour. When first trying out the hypoxia chamber, the embryos remained in hypoxic water for 6 hours, as was the procedure in [48], but in our case this led to a very high mortality among the embryos, exceeding 50%.

It proved difficult to distinguish live and dead embryos, if neither are swimming. This is a problem, because we do not want to accidentally mount embryos that are already dead on the irradiation setup. Doing so would lead to unreliable mortality figures and reduce the amount of live embryos available for further analysis after irradiation. Other indicators to quickly determine whether an embryo is alive, such as movement upon applying a jet of water by pipette, or a visibly beating heart when examined under a transmission microscope, also proved unreliable. Even when neither of these indicators were present when in hypoxia, they could reappear after the embryo had spent some time in normoxic water. Embryos that had seemed dead would then move around indistinguishably to embryos that never even received a hypoxic treatment. The optimal hypoxic treatment therefore has maximum impact on the embryo's amount of available oxygen in the circulatory system, without causing significant mortality. To find this optimum, we exposed the embryos to water with 10% oxygen saturation, and then after one hour took out 10 embryos every 15 minutes to see how many heartbeats would return after being placed in normoxic water again. The results are displayed in table 4.1.

Length of hypoxic treatment (minutes)	Heartbeats after 15 minutes	Heartbeats after 2 hours	Other observations after 2 hours
60	10/10	10/10	Embryos resumed swimming small distances
75	10/10	10/10	Embryos moved around slightly
90	10/10	10/10	Mouth and fins would visibly move
105	4/10	10/10	-
120	5/10 (after 30 minutes)	-	-

Table 4.1: Embryo responses to hypoxic treatments

Even though some data points are missing, we still see that already after 75-90 minutes in the hypoxia

chamber the embryos remain physically impacted for two hours even after leaving the hypoxic chamber. The reduced movement in this case indicates a shortage of molecular oxygen in the body, as it stops dissipating oxygen in the muscles. From this, we concluded that a hypoxic treatment of 105-120 minutes at 10% should be enough to guarantee acute hypoxia during irradiation (which could take place up to two hours after mounting). This would be the case even more, considering that during an irradiation experiment we would not put the embryos back into normoxic water, but rather pipette them with the hypoxic water to their wells. This does not mean the hypoxic treatment is continued, because when the oxygen concentration is not regulated, it will increase through diffusion, especially when aerated in small volumes during pipetting. However, the hypoxic condition of the embryos will not resolve as quickly as if they were transferred to normoxic water.

We should note that in the final radiation experiment, from which all results presented in this chapter were produced, the aliveness of the embryos was still double-checked before they were mounted. This did require pipetting the embryos from the hypoxia chamber to a petri dish to examine them under a transmission microscope, after which the ones with visible heartbeats were pipetted to the well. This aerated the water more than if it had been pipetted directly from the hypoxia chamber to the well, probably increasing the oxygen saturation to a slightly larger extent.

4.3. Mortality

A first indicator of the damage suffered by irradiation could be the mortality rate among the embryos, depicted in figure 4.2.

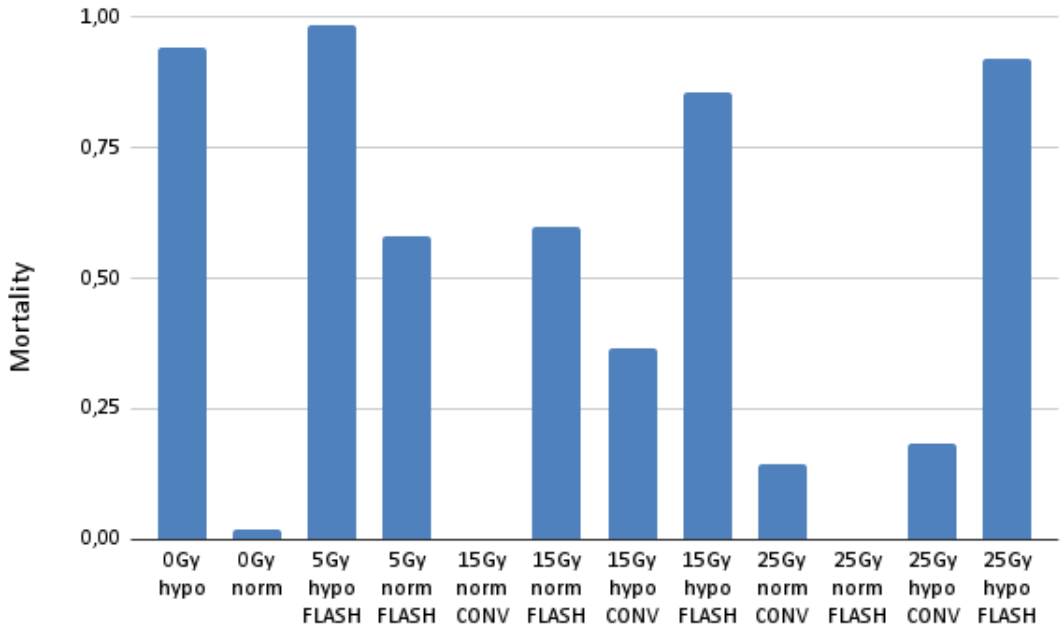

Figure 4.2: The mortality among embryos as caused by different radiation treatments.

These mortality figures, however, definitely cannot be explained by (only) the radiobiological damage suffered. Consider for example the very high mortality among the 0 Gy hypoxic group, and the relatively low mortality 25 Gy hypoxic CONV group.

It should be noted that the FLASH-irradiated samples spent a much longer time in the wells (3 hours between being mounted and being back in the incubator) than the CONV-irradiates samples (90 minutes between being mounted and being back in the incubator). This was because the radiation technicians at HollandPTC had some issues with the FLASH setup, which was beyond our control. This probably contributed to the generally much higher mortality among the FLASH groups, as compared to the

Radiation treatment	Amount of embryos in well
0 Gy hypo	67
0 Gy norm	56
5 Gy hypo FLASH	68
5 Gy norm FLASH	62
15 Gy norm CONV	44
15 Gy norm FLASH	55
15 Gy hypo CONV	40
15 Gy hypo FLASH	56
25 Gy norm CONV	48
25 Gy norm FLASH	44
25 Gy hypo CONV	49
25 Gy hypo FLASH	51

Table 4.2: The amount of embryos in a well during irradiation seems to impact the mortality

CONV groups (with the curious exception of the 25 Gy norm FLASH group, which we will discuss later). It also seems clear that among the hypoxic groups, the mortality is much higher than among the normoxic groups. This further confirms the effectiveness of the hypoxic treatment, even after the embryos are mounted. Another possible explanation for the disproportionately high mortality in some groups is the amount of embryos that were mounted in that single well. The amount of embryos in the well for each radiation treatment is depicted in table 4.2. Wells that contained more embryos seem to have experienced higher mortality rates.

Importantly, being in an overcrowded well, in hypoxic water, as well as having spent a longer time being mounted in the setup, might not only have additive effects, but also multiplicative effects. I.e., being mounted in a crowded well makes the extra time spent in the setup even more harmful. So does being in hypoxic water. A multiplicative effect of hypoxia, crowdedness, and spending a long time in the setup (because the 0 Gy controls were mounted with the FLASH samples) may explain the very high mortality among the 0 Gy hypoxic group, even though it received no dose. Likewise, it can explain the absence of mortality in the 25 Gy norm FLASH group, even though it received 25 Gy. This well contained the least amount of embryos, and was normoxic.

The precise effect of each factor described, as well as the interplay between different factors, is very hard to quantify. Therefore, it was unfortunately impossible to reliably isolate any effect of the radiation treatment from these mortality figures. Still, it does seem that in other circumstances mortality could be a useful biomarker. This is elaborated upon in the recommendations section, 5.

4.4. γ-H2AX Staining

4.4.1. Qualitative Analysis of a Sample with good Antibody Penetration

Figure 4.3 features five focal planes from an example image, one that seemed to have reasonable antibody penetration. Various anatomical features are visible, with specific signal visible in the pectoral fin, the intestine, the spinal muscles and the heart. Of these, spinal muscles were most consistently visible among all images. Therefore, they would become the object for further analysis (see section 3.7).

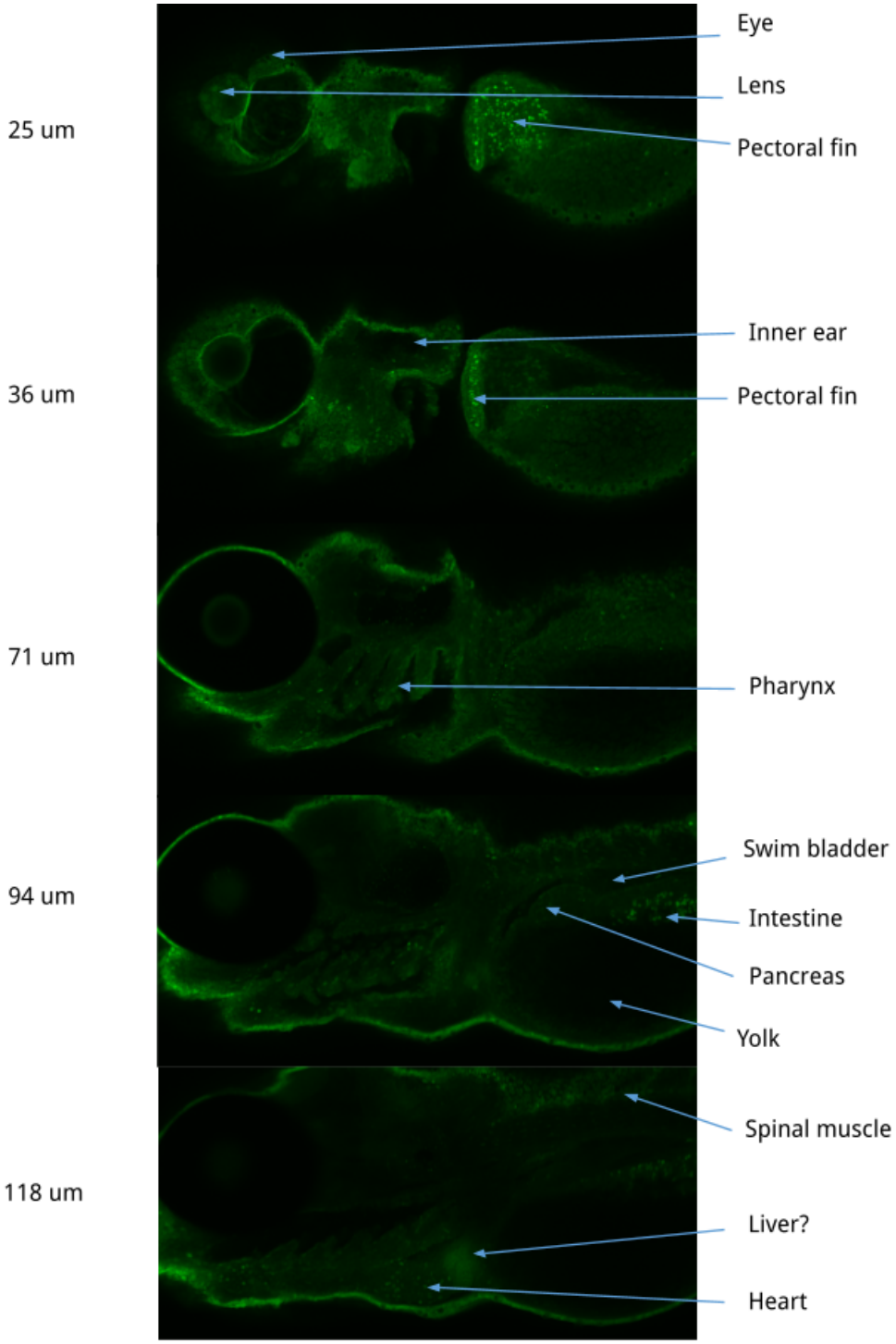

Figure 4.3: Focal planes from a Z-stack of the γ-H2AX channel of a proton irradiated embryo with good antibody penetration, with arrows pointing out recognizable anatomical features, based on the ZFIN Anatomy Atlas [58].

4.4.2. Co-localization

Unfortunately, because beam time was scarce and mortality during the irradiation procedure was high, especially for some groups, we did not acquire a lot of samples available for antibody staining for every group. Because antibody staining is also a delicate process that requires many steps, some groups could not be represented altogether. For example, we had some samples were the DAPI staining wasn't done right, which would make the samples unfit for co-localization. Also, some embryos are damaged during mounting on the glass slide before imaging.

The only dose groups that are mostly complete, and have sufficient quality images, were the 15 Gy and 25 Gy groups. Most notably, we do not have any hypoxic FLASH groups (because these were the groups with highest mortality, see section 4.3). The results of the γ-H2AX staining are displayed in figure 4.4.

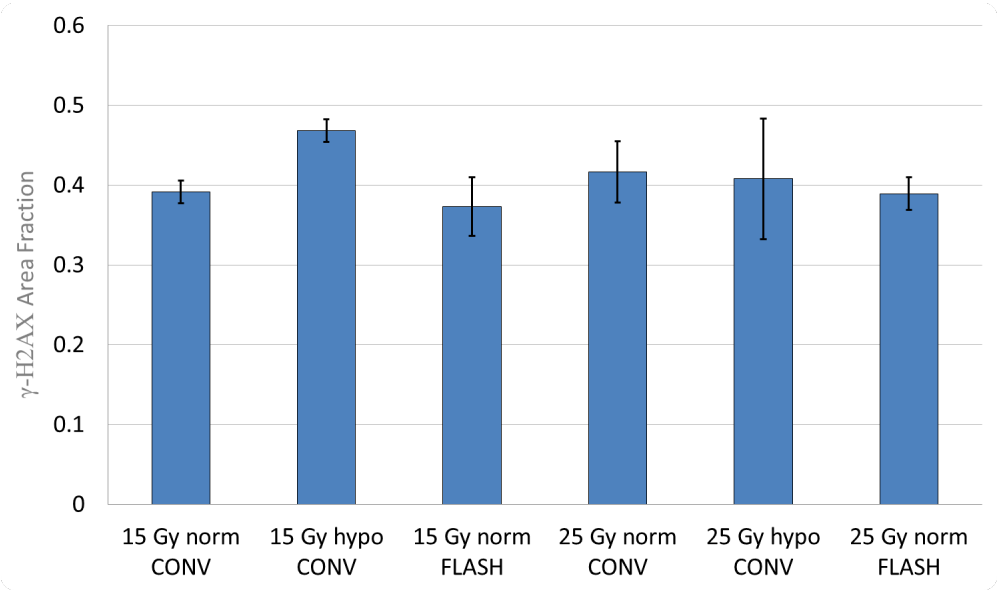

Figure 4.4: γ-H2AX area as a fraction of DAPI area. N = 3 for each group. Figure based on images presented in appendix D

The results do show that the normoxic FLASH groups have the lowest fraction, which would be in line with the hypothesis, but the differences are all within the standard deviation. Furthermore, we would expect the hypoxic CONV group to be less damaged than the normoxic CONV group, but that does not correspond with these results. In the 15 Gy case the hypoxic group appears to have suffered more DNA breaks than the normoxic group, in the 25 Gy case there is no significant difference. Most importantly, there is hardly any difference between the 15 Gy and the 25 Gy groups, even though there should be a lot more DNA breaks for 25 Gy. Especially the latter observation suggests that our method does not produce results that indicate the actual amount of radiobiological damage, in a way that allows us to compare multiple samples from different groups.

Explanations Based on the Data Considered

There are a few possible issues with both the data and the analysis. It does not seem likely that we misinterpreted non-specific signal from the γ-H2AX as specific signal, as we do see nucleus-shaped dots at specific places, that furthermore overlap with a nucleus-shaped dot in the DAPI signal. Also, our signal resembled the signal in an example image provided by the manufacturer. Possible explanations might be found contemplating whether only some of the double-stranded DNA breaks could be caused by the radiation, and other steps in the protocol also cause DNA damage.

We were only able to consider muscle tissue close to the skin, where there might be a lot of naturally occurring DNA damage. Maybe the amount of DNA breaks in vital organs deeper in the body is a better measure for radiobiological damage, but to consistently be able to image these, better antibody penetration is needed. Also, sometimes a sample did not have the right orientation. Section 5 provides suggestions on how these issues might be resolved.

Explanations Based on the Analysis

The co-localization protocol required one manual step, i.e. choosing the signal threshold. Even tough it was not possible to apply a standardized threshold, because this would remove clearly specific signal in one sample but keep autofluorescence in another, this does allow for a bias in the observer who might unconsciously make a decision partly based on how much signal 'should' remain, being inclined to make the threshold higher when there is a lot of signal and lower if there is not. Also, the protocol might not have been thorough enough. A mere threshold (even combined with the co-localization) might not

discriminate well enough between signal and noise, because specific signal is mainly recognisable by its shape, rather than by its intensity.

4.5. Simulation Results

4.5.1. Validation of the SOBP

Figure 4.5 shows the dose deposition at different penetration depths in a body of water, as produced by the energy spectrum described in Section 3.8.2. The scoring volume is described in Section 3.8.6. Unlike the homogeneity simulations, we score the energy deposit as opposed to the dose (which is energy deposit per mass). In this case, the energy deposit will more intuitively show what is happening, especially as the beam traverses different materials.

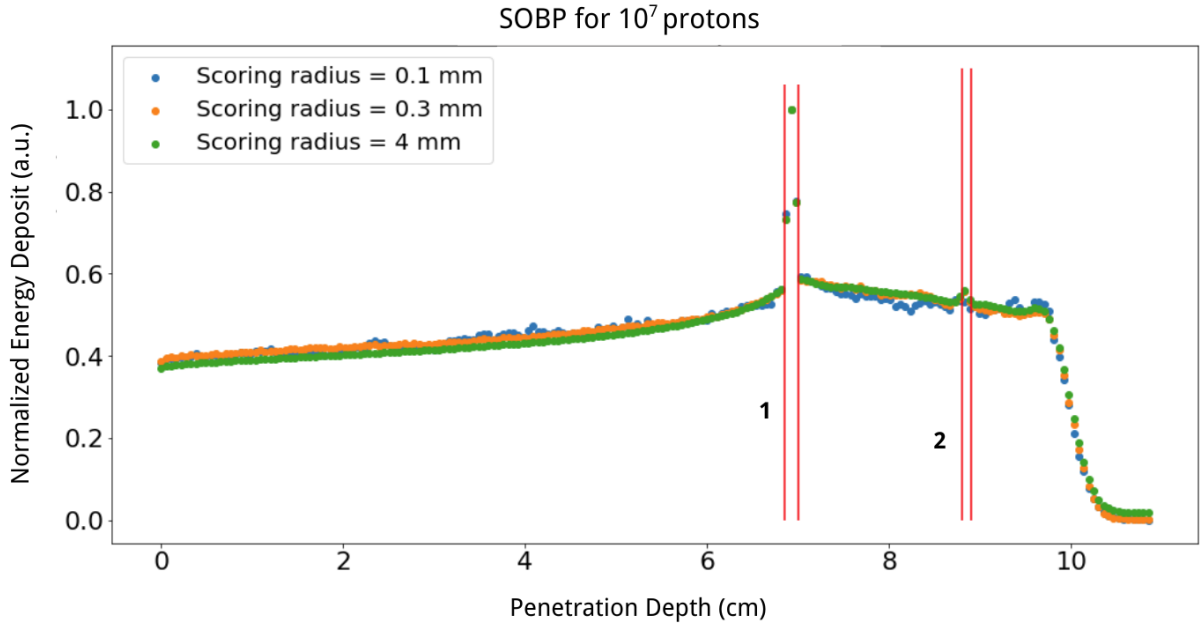

Figure 4.5: The shape of the spread-out Bragg peak in our setup 3.4. Red lines denote the positions of the lid and bottom of the well: (1) the location of the lid, (2) the location of the bottom. Embryos are always between the two inner red lines. There are orange data points between the red lines denoting the lid location, but they overlap with the green data points.

We see the SOBP starting at 6.9 cm within the medium. This corresponded to the real-life behaviour of the beam, validating the energy spectrum, which was the most important goal of this simulation. We also see that the SOBP is not entirely flat. This is probably due to lateral spreading of the beam as it traverses the WET slabs and the resin lid, because the same energy spectrum did not produce a tilted SOBP in [23]. The spreading happens because protons scatter out of the scoring volume, while fewer are scattering into it because there is air on the outside, which is much less dense. This would cause a systematic slightly lower energy deposit at the end than at the front.

Peaks in Resin Lid and Polystyrene Bottom

The peaks in energy deposition in the lid and the bottom of the well require an explanation. Polystyrene and water have a very similar mass stopping power (i.e. the stopping power per density) for < 116 MeV protons (at 116 MeV, 6.401 MeV cm^2/g and 6.535 MeV cm^2/g, respectively [59]), but polystyrene has a density of 1.06 g/cm^3 and Géant4 water 0.997 g/cm^3. Multiplying the mass stopping power by density leads to the polystyrene having a stopping power of 6.785 MeV/cm, and the water a stopping power of 6.515 MeV/cm. The slightly higher polystyrene stopping power explains the peak in energy deposit at the bottom of the well.

Epoxy resin has a higher proton stopping power than both water and polystyrene, already exceeding 7 MeV/cm for 116 MeV protons [60]. This explains the even higher peak for Resin. The high scores might

look stochastic, due to all the white space between the few data points denoting the energy deposits in the resin lid, but in reality form a peak similar to the peak in the polystyrene bottom, only higher.

Stochastic Behaviour in Small Scoring Volumes
For a scoring volume with a radius of 0.1 mm perpendicular to the beam, we see the energy deposit starting to become more stochastic, as less protons enter the scoring volume as it gets smaller, reducing the applicability of the law of large numbers. In the homogeneity simulations, we want to be sure that enough protons enter the voxel volumes to avoid large uncertainties in the scores. The scoring volume used in the homogeneity simulations is 1458 mm^3 (9x9x18mm), divided in 2500 (25x25x4) voxels, leading to each voxel having a volume of 0.5832 mm^3. Fortunately, the bin size for which we started seeing stochastic behaviour is much smaller: 1/200th of a cylinder with radius 0.1 mm and length 110 mm, i.e. 0.01728 mm^3. The cuboid voxels are more comparable to the 4 mm scoring volume bins, which have a volume of 0.2765 mm^3. They produced a flat SOBP, while still being smaller than our cuboid voxels in the homogeneity simulations.

This is evidence that 10^7 histories is a sufficient particle number for the scoring resolution we aim to get in the homogeneity simulations. However, we cannot compare the voxel sizes one on one. The scoring volumes in both simulations are binned (i.e. divided into voxels) differently: cuboid voxels versus cylinder slices. The reason for this difference being, that in this simulation we were mostly interested in the SOBP, but when we are interested in the homogeneity within the well, we also want to divide the scoring volume perpendicularly to the beam to see the difference between the centre and the edges of the well, and are not as interested in differences between the front and the back of the well. We still are, but can use a lower resolution. Therefore, we also used other methods to determine the effect of the particle number on the simulation's result.

4.5.2. Determining the Particle Number Required for the Desired Resolution

To determine what simulation size gives us the best trade-off between speed/computational power and minimizing artifacts of the limited particle number, we ran our homogeneity simulation with different particle numbers ('histories') and considered the results, which are displayed in figure 4.6.

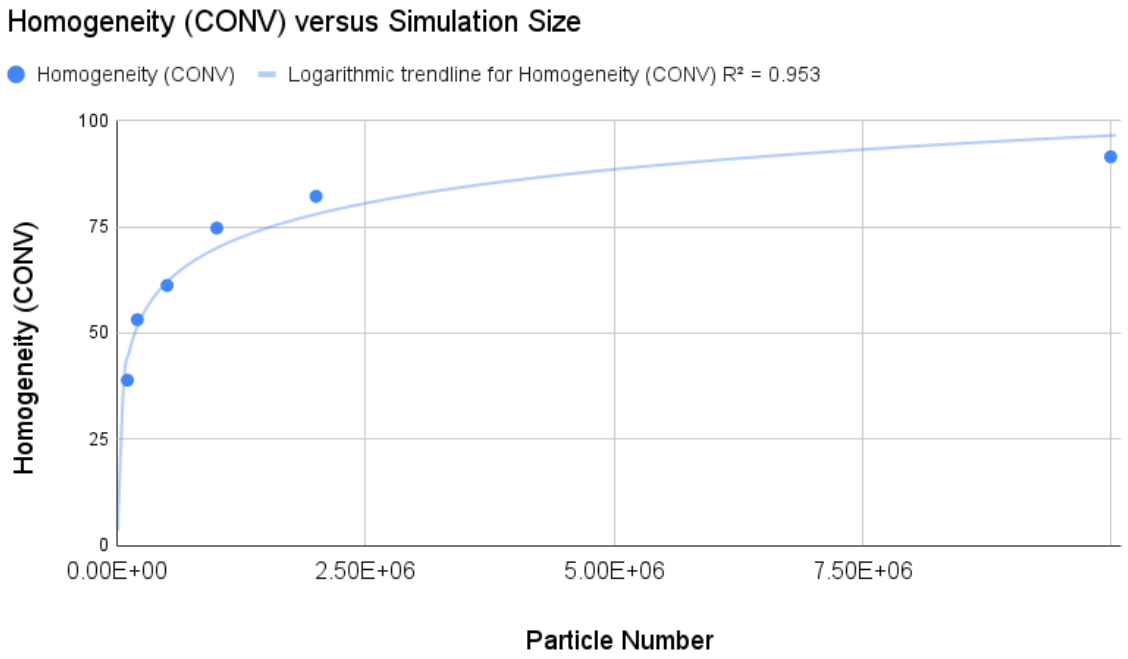

Figure 4.6: The dose homogeneity in the well (based on the highest scoring and lowest-scoring voxel) increases with the particle number

We see the homogeneity (calculated using Equation 3.1) increase with the particle number. This was expected, as extreme stochastic results become rarer and rarer as the particle number increases. The homogeneity reaches an asymptote to which we want to be sufficiently close. In an ideal case, with a perfectly flat SOBP and no perturbations by the medium whatsoever, we would expect the homogeneity to tend to 100%. However, we already know this is not the case, so we should not expect this. Also considering:

- 10^7 protons already produce a homogeneity of 91.5%
- Between the last two data points, the homogeneity increased with 'only' a factor of 1.11 (or 9 percentage points) while the particle size increased with a factor 5
- The homogeneity will only increase slower and slower closer to the asymptote
- We do not need to be infinitesimally close to the asymptote, before we can consider systematic patterns emerging in local dose differences (like voxels at the edges consistently getting a lower dose), which become apparent even if the total homogeneity of the entire well is still relatively low.

Based on the results of figure 4.6 and above remarks, we decided that 10^7 histories is an appropriate and practical amount for our resolution.

4.5.3. CONV Homogeneity

Figure 4.7 shows the dose profile at different depths in the well, as described in section 3.8.5.

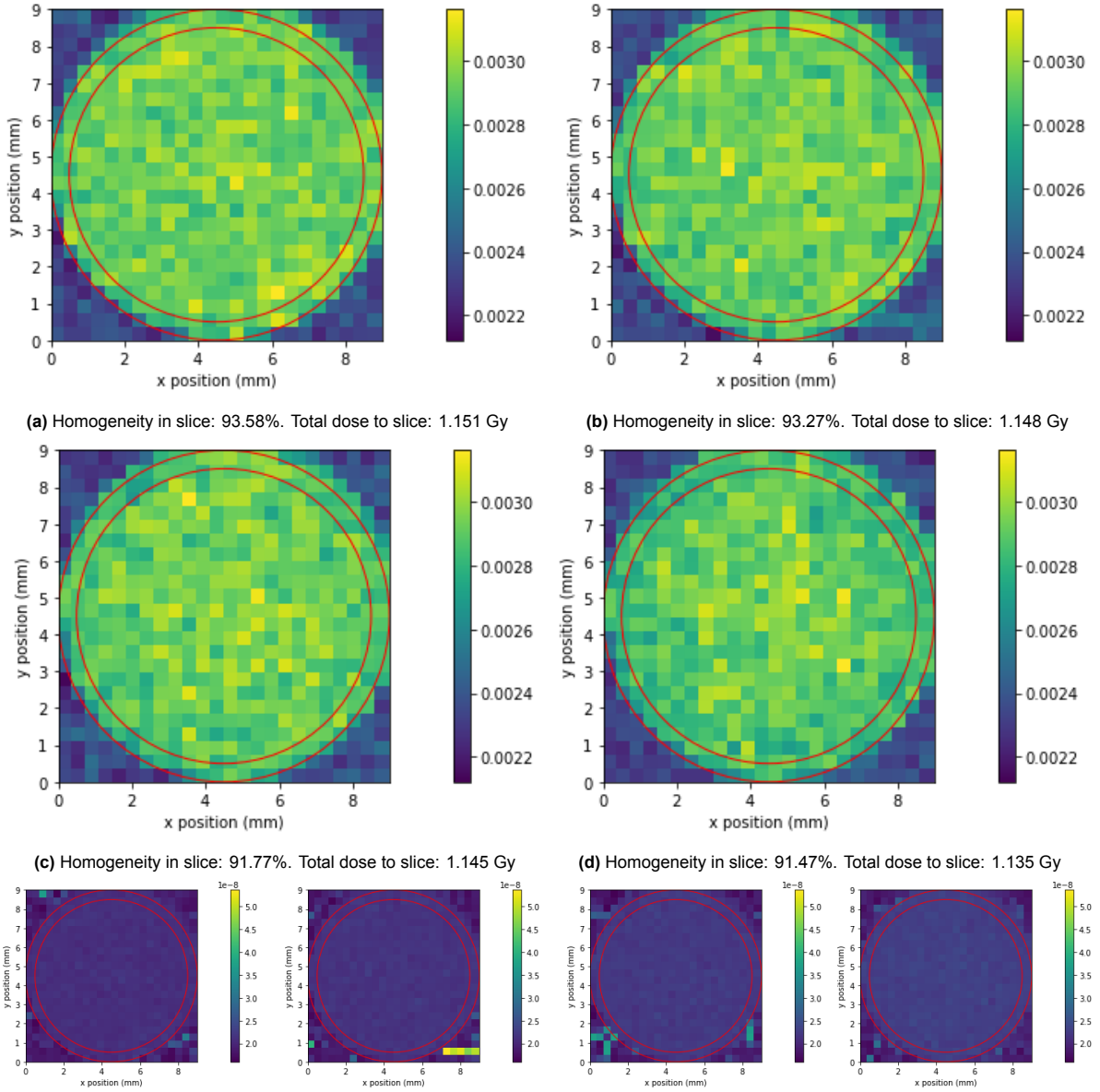

(a) Homogeneity in slice: 93.58%. Total dose to slice: 1.151 Gy

(b) Homogeneity in slice: 93.27%. Total dose to slice: 1.148 Gy

(c) Homogeneity in slice: 91.77%. Total dose to slice: 1.145 Gy

(d) Homogeneity in slice: 91.47%. Total dose to slice: 1.135 Gy

(e) Standard deviations in slice **(a)**

(f) Standard deviations in slice **(b)**

(g) Standard deviations in slice **(c)**

(h) Standard deviations in slice **(d)**

Figure 4.7: The dose deposition profile at different depths in a CONV-irradiated well. Color of represented voxel denotes dose score. Description below subfigure lists dose sum of all voxels in that slice, and homogeneity based on the highest and lowest scoring voxel in that slice. Total homogeneity across all slices = 91.47%.

In the CONV results, we do not see a striking source of heterogeneity in each individual slice. There does not seem to be anything noteworthy going on at the edges. We do however see both the homogeneity ánd the dose sum of a slice decrease as we look further into the well, with the bottom of the well receiving 98.61% of the dose received by the top (1.135 Gy versus 1.151 Gy). This is in accordance with our expectations based on figure 4.5, where we also see the energy deposition slightly decrease.

Even though we cannot say for certain to what point the homogeneity numbers would increase further (if we were to run the simulation with even more histories), we established that any systematic dose heterogeneity should become apparent in the simulation. It does seem that heterogeneity in the dose distribution is primarily caused by a few voxels randomly having received a larger or smaller dose, rather

than any systematic effect (except the slight decrease described above). The absence of significant systematic heterogeneity, a homogeneity of 91.47% across all slices, which furthermore seems to be primarily caused by stochastic differences related to the limited particle number, gives no sufficient justification to modify the radiation setup. This would be very difficult, as none of the components are easily replaced or modified.

4.5.4. Bare Beam FLASH Homogeneity

Figure 4.8 shows the dose profile at different depths in the well, as described in section 3.8.5.

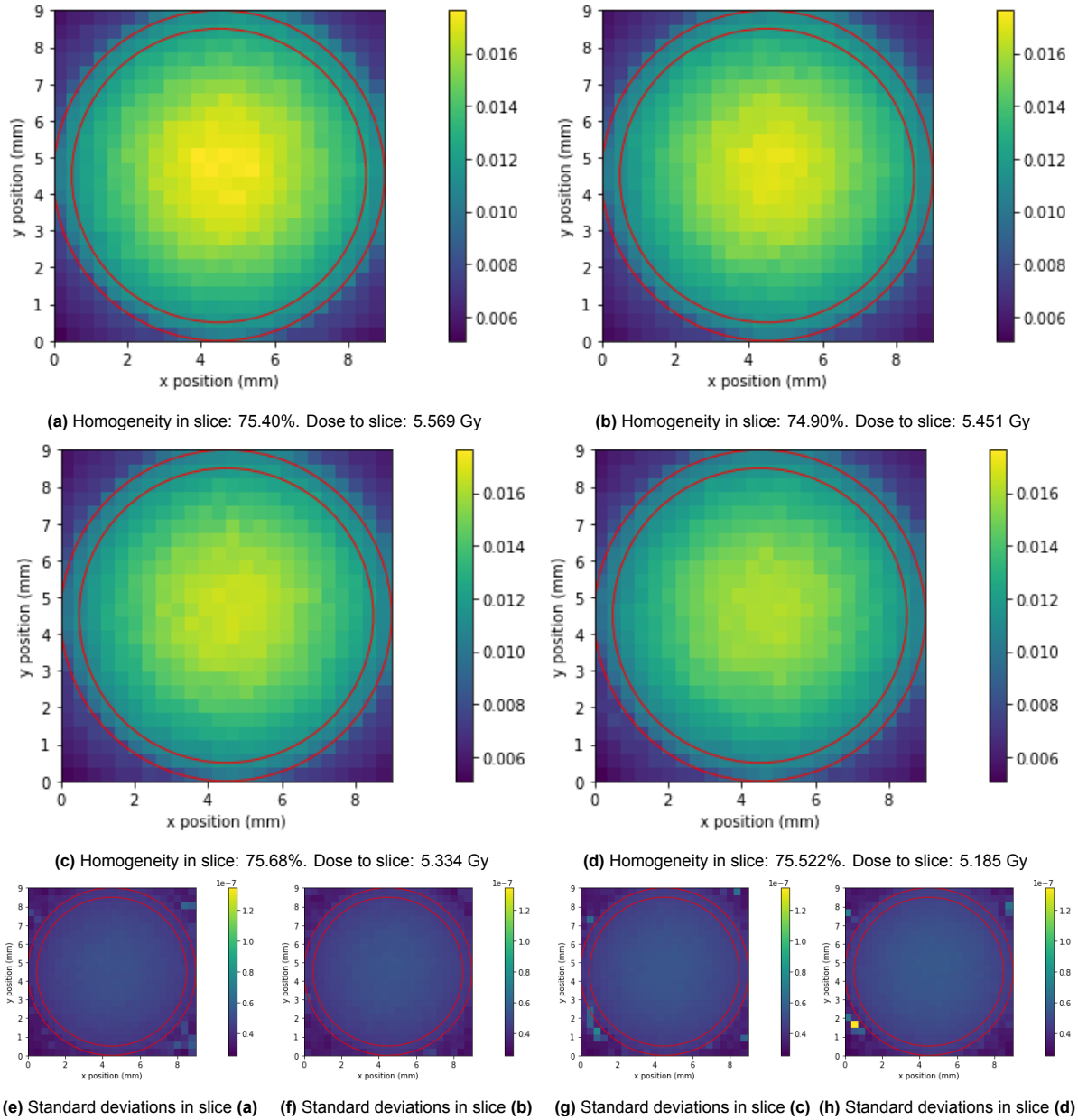

(a) Homogeneity in slice: 75.40%. Dose to slice: 5.569 Gy

(b) Homogeneity in slice: 74.90%. Dose to slice: 5.451 Gy

(c) Homogeneity in slice: 75.68%. Dose to slice: 5.334 Gy

(d) Homogeneity in slice: 75.522%. Dose to slice: 5.185 Gy

(e) Standard deviations in slice **(a)** **(f)** Standard deviations in slice **(b)** **(g)** Standard deviations in slice **(c)** **(h)** Standard deviations in slice **(d)**

Figure 4.8: The dose deposition profile at different depths of a FLASH-irradiated well. Color of represented voxel denotes dose score. Description below subfigure lists dose sum of all voxels in that slice, and homogeneity based on the highest and lowest scoring voxel in that slice. Total homogeneity across all slices = = 71.66%.

In the FLASH results, we clearly see the effect of using a Gaussian-shaped beam rather than a flat beam. Dose differences between the centre and the edges of the beam are the most important source of heterogeneity. We see a slight decrease in dose deposition as we go further into the well, very similar to the CONV case.

The total homogeneity across all slices remained at 71.66% in the bare beam FLASH case. We decided this homogeneity was too low, as this means a nominal dose of 25 Gy could in reality be a 18 Gy dose. Such uncertainty, in combination with the generally limited amount of samples, would make it too difficult to draw conclusions from any difference in radiobiological damage between CONV and FLASH groups. We therefore decided to not use the unscattered pencil beam, but still scatter the beam a little bit as described in section 3.4.2. Upon request, we received the results of a quick measurement of the half-scattered lateral beam profile, i.e. the beam profile after traversing the setup with only the scattering foil and not the dual scattering ring. They are displayed in figure 4.9. The corresponding beam characteristics used as an input for the simulation were previously described in section 3.8.2.

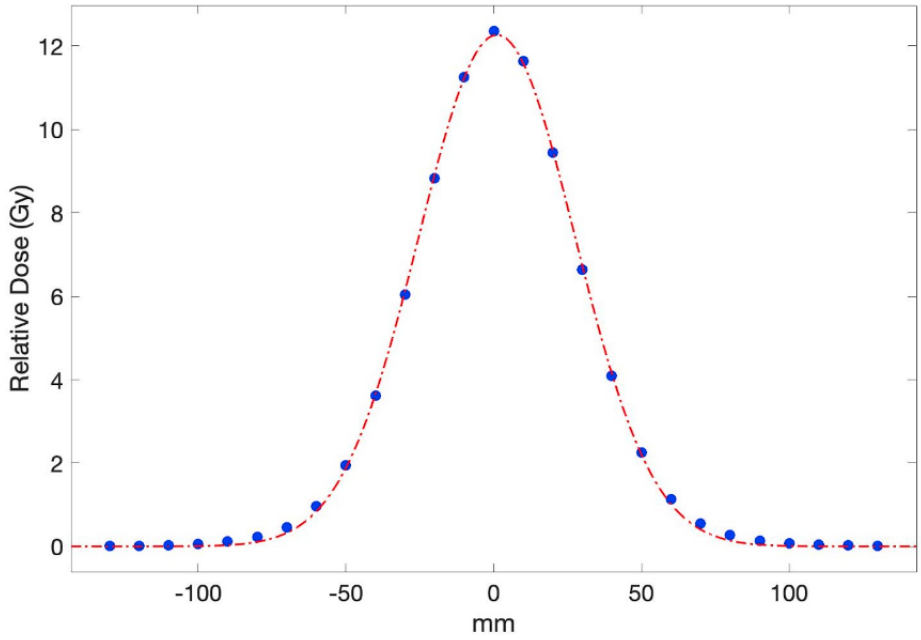

Figure 4.9: The lateral beam profile of the half-scattered beam. The position spread, i.e. the standard deviation of the distance from the centre, is 29.55mm.

4.5.5. Half-Scattered FLASH Homogeneity

Figure 4.10 displays the dose profile at different depths in the well for the half-scattered FLASH beam.

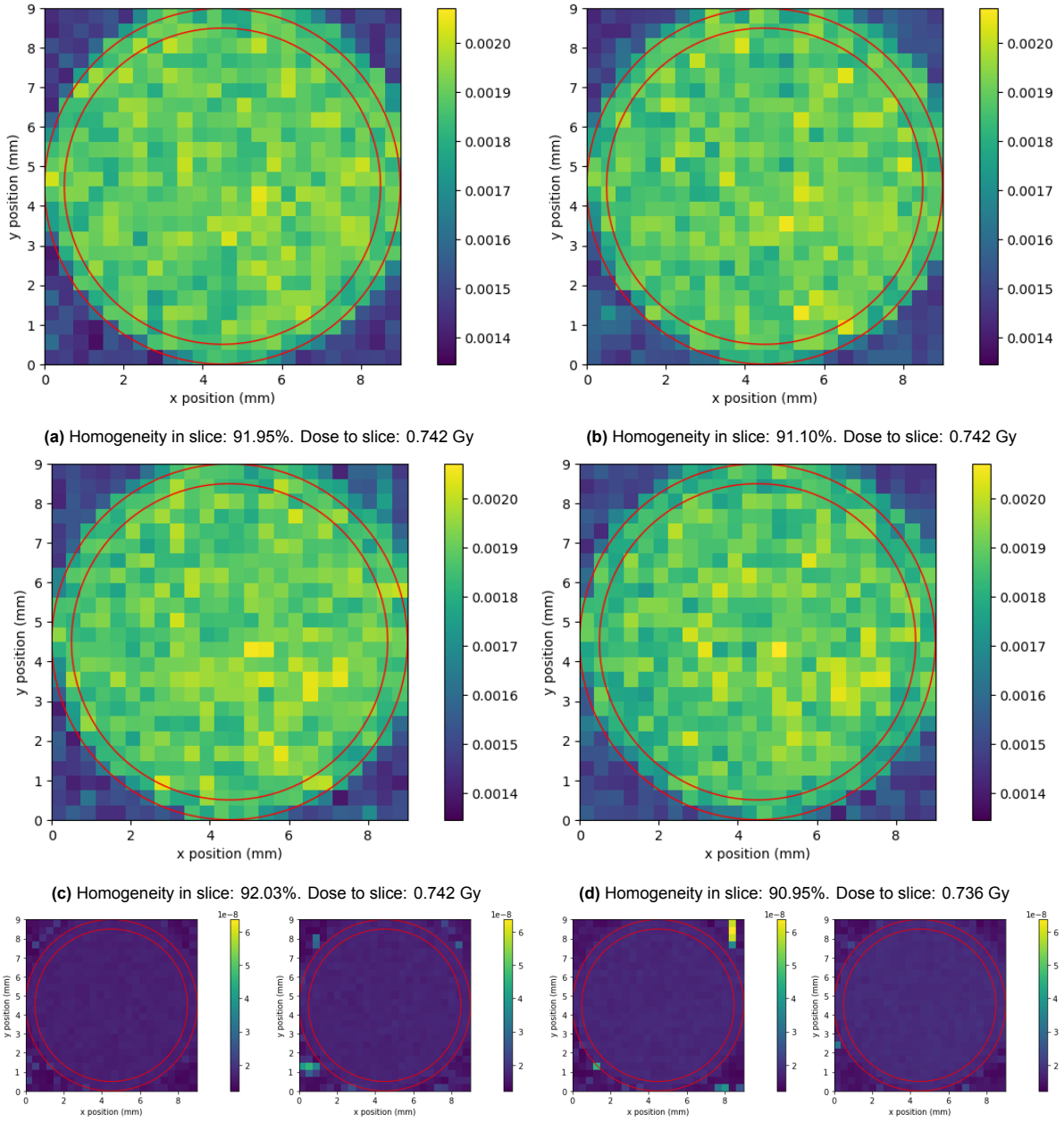

(a) Homogeneity in slice: 91.95%. Dose to slice: 0.742 Gy

(b) Homogeneity in slice: 91.10%. Dose to slice: 0.742 Gy

(c) Homogeneity in slice: 92.03%. Dose to slice: 0.742 Gy

(d) Homogeneity in slice: 90.95%. Dose to slice: 0.736 Gy

(e) Standard deviations in slice **(a)**

(f) Standard deviations in slice **(b)**

(g) Standard deviations in slice **(c)**

(h) Standard deviations in slice **(d)**

Figure 4.10: The dose deposition profile at different depths of a FLASH-irradiated well. Color of represented voxel denotes dose score. Description below subfigure lists dose sum of all voxels in that slice, and homogeneity based on the highest and lowest scoring voxel in that slice. Total homogeneity across all slices = 90.72%.

As expected, the homogeneity did greatly increase compared to the bare beam, to a level comparable with the CONV setup. This confirmed that the proposed FLASH setup as described in 3.4.2 is viable. It also confirmed that we do need to use a 96-well plate as opposed to the 24 well plate with larger wells, which was used in some initial experiments.

4.5.6. Dose Outside the Well

It can also be noted that there is almost no dose in the air outside the well. This is not because the beam shape perfectly matches the well, but just because the dose outside the well is much lower, as

the outside of the well consists of air and not water. Air has a much lower mass stopping power than water, due to water molecules' dipole moment.

5

Conclusions

Creating the Hypoxic Condition

The self-regulating hypoxic aquarium worked adequately and could reduce the oxygen saturation of its water content to the (initially) desired 8%. When not being actively oxygenated by stirring, hypoxic water would re-oxygenate only relatively slowly even after nitrogen dispersion stopped. One hour after oxygen regulation was stopped, oxygen saturation would have increased from below 10% to around 30%, in situations without active oxygenation.

Moreover, embryos would show visible symptoms of hypoxia (reduced movement and absence of a visible heartbeat) even two hours after being transferred back to normoxic water. This would apply to embryos who had received a hypoxic treatment longer than 75 minutes, and the symptoms would be more prevalent for embryos with longer treatments.

Even though it proved difficult to quantify the exact level of hypoxia experienced by the embryo tissue at the moment of irradiation, the results described above together do indicate that the embryos in the hypoxic groups definitely should have experienced an oxygen deficiency during irradiation.

Simulating Dose Distribution in the Well

We were able to computationally model the geometry of our setup, as well as the characteristics describing our proton beam, based on earlier experiments and simulations. We found a simulation consisting of 10^7 histories to be sufficient for our purposes. Simulations of this size yielded a dose homogeneity of 91.47% for the CONV setup, 71.66% for the bare beam FLASH setup, and 90.72% for the half-scattered FLASH setup. Except for the bare beam FLASH setup, heterogeneity in the dose distribution seemed to be primarily caused by a few voxels randomly having received a larger or smaller dose, rather than any systematic effect. These simulation results convinced us to not use the bare beam FLASH setup and reinforced our decision to use wells with a smaller diameter.

Mortality

Mortality turned out not to be a reliable biomarker for radiobiological damage, in our experiments. Other factors contributing to mortality besides radiation (hypoxia, crowdedness of the well, time spent in the well) were not consistent between all the groups, usually beyond our control. Because these factors differed, and their effects are multiplicative, it was not possible to isolate the effect of the radiation treatment on the mortality.

γ-H2AX Staining

Two dose groups yielded a sufficient amount of samples (N=3 per subgroup) to meaningfully compare them, the 15 Gy and the 25 Gy groups. We isolated a piece of muscle tissue from each sample, applied an intensity threshold and co-localized the remaining signal with the DAPI signal to remove any signal not coinciding with the location of an actual nucleus. The amount of remaining signal as a fraction of the DAPI signal was supposed to be a measure of the radiobiological damage. However, the differences were hardly significant (even between the 15 Gy and 25 Gy groups), and those that were

made no biological sense. Possible explanations include the muscle tissue not being a reliable organ to investigate, or a systematic flaw in the image analysis.

Recommendations

Antibody Staining

It is probably possible to extend the digestion in collagenase, prior to the actual staining. Even though we already increased the digestion time from 30 to 60 minutes, we did not experience any disadvantage, while it did improve our image quality. Many problems encountered later, during image analysis, boiled down to not consistently seeing specific γ-H2AX signal in internal organs. Better antibody penetration could greatly increase the quality of the data and possibilities for analysis.
Another recommendation would be to find a way to mount all samples in the same orientation on the glass slide. We mounted the embryos in the position in which they were most stable, because reorienting them had a high risk of damaging the samples, and some would just roll back into their previous position anyway, sometimes even after mounting, so it didn't seem worthwhile. If it were possible to mechanically fix the embryos in a certain orientation, it would improve the consistency in the images, making it easier to find a piece of tissue to compare between samples.

Simulations

The FLASH beam, having only been installed during the course of this thesis, had not yet been as properly characterised as the CONV beam at the time of our experiments. Consequently, we used some of the CONV beam characteristics to model the FLASH beam, specifically the initial angular spread. However, the FLASH beam has since also been characterised as the subject of another (yet unpublished, but available to the HollandPTC radiation technicians) thesis project. Therefore, in any follow-up simulations, the FLASH beam model should be updated accordingly.

Irradiation

In a further experiment, an effort should be made to limit and standardize the amount of embryos mounted per well. We hardly limited the amount of embryos per well, seeing little downside to trying to irradiate as many samples as possible. We also made no special effort making sure the amount of embryos per well was comparable everywhere. We distributed the embryos only approximately, by eye, without counting each individual embryo, which would have been time consuming in an already intensive part of the experiment. In practice, this led to the least occupied well containing 40 fish while the most occupied well contained 68. Considering this probably influenced mortality, we would recommend aiming for a maximum of 40 fish per well.
It should also be possible to standardize the time spent mounted, another factor likely influencing mortality. The main reason we could not do this concerned the radiation technicians' inexperience with the new FLASH setup.
Only the mortality causing factor of being mounted in hypoxic water seems unavoidable, as it is inherent to the project. However, with the right control groups and the absence of the other factors this effect could probably be quantified and corrected for. If these improvements can all be implemented, mortality might actually become a useful biomarker.

References

[1] Jacques Ferlay et al. “Cancer statistics for the year 2020: An overview”. In: *International journal of cancer* 149.4 (2021), pp. 778–789.

[2] Eduardo Rosenblatt, Oscar Acuña, and May Abdel-Wahab. “The challenge of global radiation therapy: an IAEA perspective”. In: *International Journal of Radiation Oncology, Biology, Physics* 91.4 (2015), pp. 687–689.

[3] Steven van de Water et al. “Towards FLASH proton therapy: the impact of treatment planning and machine characteristics on achievable dose rates”. In: *Acta Oncologica* 58.10 (2019). PMID: 31241377, pp. 1463–1469. DOI: 10.1080/0284186X.2019.1627416. eprint: https://doi.org/10.1080/0284186X.2019.1627416. URL: https://doi.org/10.1080/0284186X.2019.1627416.

[4] Jean Bourhis et al. “Clinical translation of FLASH radiotherapy: Why and how?” In: *Radiotherapy and Oncology* 139 (2019), pp. 11–17.

[5] Eric S Diffenderfer et al. “Design, implementation, and in vivo validation of a novel proton FLASH radiation therapy system”. In: *International Journal of Radiation Oncology* Biology* Physics* 106.2 (2020), pp. 440–448.

[6] Qixian Zhang et al. “Flash investigations using protons: Design of delivery system, preclinical setup and confirmation of flash effect with protons in animal systems”. In: *Radiation Research* 194.6 (2020), pp. 656–664.

[7] Elke Beyreuther et al. “Feasibility of proton FLASH effect tested by zebrafish embryo irradiation”. In: *Radiotherapy and Oncology* 139 (2019). FLASH radiotherapy International Workshop, pp. 46–50. ISSN: 0167-8140. DOI: https://doi.org/10.1016/j.radonc.2019.06.024. URL: https://www.sciencedirect.com/science/article/pii/S0167814019329640.

[8] Manuela Buonanno, Veljko Grilj, and David J. Brenner. “Biological effects in normal cells exposed to FLASH dose rate protons”. In: *Radiotherapy and Oncology* 139 (2019). FLASH radiotherapy International Workshop, pp. 51–55. ISSN: 0167-8140. DOI: https://doi.org/10.1016/j.radonc.2019.02.009. URL: https://www.sciencedirect.com/science/article/pii/S0167814019300763.

[9] Pierre Montay-Gruel et al. “Long-term neurocognitive benefits of FLASH radiotherapy driven by reduced reactive oxygen species”. In: *Proceedings of the National Academy of Sciences* 116.22 (2019), pp. 10943–10951. ISSN: 0027-8424. DOI: 10.1073/pnas.1901777116. eprint: https://www.pnas.org/content/116/22/10943.full.pdf. URL: https://www.pnas.org/content/116/22/10943.

[10] Eric S. Diffenderfer et al. “The current status of preclinical proton FLASH radiation and future directions”. In: *Medical Physics* 49.3 (2022), pp. 2039–2054. DOI: https://doi.org/10.1002/mp.15276. eprint: https://aapm.onlinelibrary.wiley.com/doi/pdf/10.1002/mp.15276. URL: https://aapm.onlinelibrary.wiley.com/doi/abs/10.1002/mp.15276.

[11] Thomas E Schmid et al. “Relative biological effectiveness of pulsed and continuous 20 MeV protons for micronucleus induction in 3D human reconstructed skin tissue”. In: *Radiotherapy and Oncology* 95.1 (2010), pp. 66–72.

[12] Susanne Auer et al. “Survival of tumor cells after proton irradiation with ultra-high dose rates”. In: *Radiation Oncology* 6.1 (2011), pp. 1–8.

[13] TE Schmid et al. “No evidence for a different RBE between pulsed and continuous 20 MeV protons”. In: *Radiation research* 172.5 (2009), pp. 567–574.

[14] V Grilj et al. “Proton irradiation platforms for preclinical studies of high-dose-rate (FLASH) effects at RARAF”. In: *Radiation Research* 194.6 (2020), pp. 646–655.

[15] Shannon Cunningham et al. “FLASH proton pencil beam scanning irradiation minimizes radiation-induced leg contracture and skin toxicity in mice”. In: *Cancers* 13.5 (2021), p. 1012.

[16] O Zlobinskaya et al. “The effects of ultra-high dose rate proton irradiation on growth delay in the treatment of human tumor xenografts in nude mice”. In: *Radiation research* 181.2 (2014), pp. 177–183.

[17] Gabriel Adrian et al. “The FLASH effect depends on oxygen concentration”. In: *The British Journal of Radiology* 93.1106 (2020). PMID: 31825653, p. 20190702. DOI: 10.1259/bjr.20190702. eprint: https://doi.org/10.1259/bjr.20190702. URL: https://doi.org/10.1259/bjr.20190702.

[18] Mirna El Khatib et al. “Ultrafast Tracking of Oxygen Dynamics During Proton FLASH”. In: *International Journal of Radiation Oncology*Biology*Physics* 113.3 (2022), pp. 624–634. ISSN: 0360-3016. DOI: https://doi.org/10.1016/j.ijrobp.2022.03.016. URL: https://www.sciencedirect.com/science/article/pii/S0360301622002498.

[19] Daria Boscolo et al. “May oxygen depletion explain the FLASH effect? A chemical track structure analysis”. In: *Radiotherapy and Oncology* 162 (2021), pp. 68–75.

[20] Xu Cao et al. “Quantification of oxygen depletion during FLASH irradiation in vitro and in vivo”. In: *International Journal of Radiation Oncology* Biology* Physics* 111.1 (2021), pp. 240–248.

[21] Adeel Kaiser et al. “Proton therapy delivery and its clinical application in select solid tumor malignancies”. In: *JoVE (Journal of Visualized Experiments)* 144 (2019), e58372.

[22] Arabinda Kumar Rath and Narayan Sahoo. *Particle radiotherapy: Emerging technology for treatment of cancer*. Springer, 2016.

[23] A.E. Meijer. “Back to the Future: Towards Ridge Filters in Clinical FLASH Proton Therapy Treatment Planning for Neuro-ONcological Targets”. In: *TU Delft Repository* (June 2021).

[24] Annalisa Patriarca et al. “Experimental Set-up for FLASH Proton Irradiation of Small Animals Using a Clinical System”. In: *International Journal of Radiation Oncology Biology Physics* 102.3 (2018), pp. 619–626. ISSN: 0360-3016. DOI: https://doi.org/10.1016/j.ijrobp.2018.06.403. URL: https://www.sciencedirect.com/science/article/pii/S0360301618314044.

[25] Marta Rovituso. “Fragmentation and lateral scattering of 120 and 200 MeV/u 4He ions on water targets”. In: (2016).

[26] María del Henar Rituerto Prieto. “Passive Beam Field Characterization for Application in Radiobiology”. In: *TU Delft Repository* (Sept. 2020).

[27] Harald Paganetti. “Nuclear interactions in proton therapy: dose and relative biological effect distributions originating from primary and secondary particles”. In: *Physics in Medicine & Biology* 47.5 (2002), p. 747.

[28] Joseph D Wilson et al. “Ultra-high dose rate (FLASH) radiotherapy: Silver bullet or fool’s gold?” In: *Frontiers in oncology* 9 (2020), p. 1563.

[29] Jean Bourhis et al. “Treatment of a first patient with FLASH-radiotherapy”. In: *Radiotherapy and Oncology* 139 (2019). FLASH radiotherapy International Workshop, pp. 18–22. ISSN: 0167-8140. DOI: https://doi.org/10.1016/j.radonc.2019.06.019. URL: https://www.sciencedirect.com/science/article/pii/S0167814019329597.

[30] Vincent Favaudon et al. “Ultrahigh dose-rate FLASH irradiation increases the differential response between normal and tumor tissue in mice”. In: *Science translational medicine* 6.245 (2014), 245ra93–245ra93.

[31] Omar Desouky, Nan Ding, and Guangming Zhou. “Targeted and non-targeted effects of ionizing radiation”. In: *Journal of Radiation Research and Applied Sciences* 8.2 (2015), pp. 247–254.

[32] DL Bailey et al. “Nuclear Medicine Physics: A Handbook for Teachers and Students. Endorsed by: American Association of Physicists in Medicine (AAPM), Asia–Oceania Federation of Organizations for Medical Physics (AFOMP), Australasian College of Physical Scientists and Engineers in Medicine (ACPSEM), European Federation of Organisations for Medical Physics (EFOMP), Federation of African Medical Physics Organisations (FAMPO), World Federation of Nuclear Medicine and Biology (WFNMB)”. In: (2014).

[33] Anna A. Friedl et al. “Radiobiology of the FLASH effect”. In: *Medical Physics* n/a.n/a (). DOI: https://doi.org/10.1002/mp.15184. eprint: https://aapm.onlinelibrary.wiley.com/doi/pdf/10.1002/mp.15184. URL: https://aapm.onlinelibrary.wiley.com/doi/abs/10.1002/mp.15184.

[34] David Robert Grimes and Mike Partridge. “A mechanistic investigation of the oxygen fixation hypothesis and oxygen enhancement ratio”. In: *Biomedical physics & engineering express* 1.4 (2015), p. 045209.

[35] Nicolas Le May, Jean-Marc Egly, and Frédéric Coin. “True lies: the double life of the nucleotide excision repair factors in transcription and DNA repair”. In: *Journal of nucleic acids* 2010 (2010).

[36] Pawan Kumar Maurya. “Chapter 10 - Animal Biotechnology as a Tool to Understand and Fight Aging”. In: *Animal Biotechnology*. Ed. by Ashish S. Verma and Anchal Singh. San Diego: Academic Press, 2014, pp. 177–191. ISBN: 978-0-12-416002-6. DOI: https://doi.org/10.1016/B978-0-12-416002-6.00010-9. URL: https://www.sciencedirect.com/science/article/pii/B9780124160026000109.

[37] J.P. Kehrer, J.D. Robertson, and C.V. Smith. “1.14 - Free Radicals and Reactive Oxygen Species”. In: *Comprehensive Toxicology (Second Edition)*. Ed. by Charlene A. McQueen. Second Edition. Oxford: Elsevier, 2010, pp. 277–307. ISBN: 978-0-08-046884-6. DOI: https://doi.org/10.1016/B978-0-08-046884-6.00114-7. URL: https://www.sciencedirect.com/science/article/pii/B9780080468846001147.

[38] Dieter Schardt, Thilo Elsässer, and Daniela Schulz-Ertner. “Heavy-ion tumor therapy: Physical and radiobiological benefits”. In: *Reviews of modern physics* 82.1 (2010), p. 383.

[39] M Thorne. “Modelling radionuclide transport in the environment and calculating radiation doses”. In: *Radionuclide Behaviour in the Natural Environment*. Elsevier, 2012, pp. 517–569.

[40] C Clifton Ling et al. “Oxygen diffusion into mammalian cells following ultrahigh dose rate irradiation and lifetime estimates of oxygen-sensitive species”. In: *Radiation research* 76.3 (1978), pp. 522–532.

[41] James Jonkman et al. “Tutorial: guidance for quantitative confocal microscopy”. In: *Nature protocols* 15.5 (2020), pp. 1585–1611.

[42] Joao Seco and Frank Verhaegen. *Monte Carlo techniques in radiation therapy*. CRC press Boca Raton, FL: 2013.

[43] Leland Lavele Carter and Edmond Darrell Cashwell. *Particle-transport simulation with the Monte Carlo method*. Tech. rep. Los Alamos Scientific Lab., N. Mex.(USA), 1975.

[44] Sea Agostinelli et al. “GEANT4—a simulation toolkit”. In: *Nuclear instruments and methods in physics research section A: Accelerators, Spectrometers, Detectors and Associated Equipment* 506.3 (2003), pp. 250–303.

[45] S. Incerti R. Capra Z. Francis and G. Montarou. “Geant4 Simulation of Very Low Energy Electromagnetic Interactions”. In: *Spenvis & Geant4 Workshop* (2005).

[46] The Zebrafish Information Network. *ZFIN*. 2020. URL: https://zfin.org/ZDB-GENO-960809-7 (visited on 05/18/2022).

[47] Monte Westerfield. “The zebrafish book: a guide for the laboratory use of zebrafish”. In: *http://zfin.org/zf_info/zfbook/zfbk.html* (2000).

[48] Pegah Rouhi et al. “Hypoxia-induced metastasis model in embryonic zebrafish”. In: *Nature protocols* 5 (Dec. 2010), pp. 1911–8. DOI: 10.1038/nprot.2010.150.

[49] Uli Weber and Gerhard Kraft. “Design and construction of a ripple filter for a smoothed depth dose distribution in conformal particle therapy”. In: *Physics in Medicine & Biology* 44.11 (1999), p. 2765.

[50] Adam Joules. *96 Well Plate, Flat Bottom, Standard*. 2019. URL: https://grabcad.com/library/96-well-plate-flat-bottom-standard-1.

[51] M. Rovituso. *Personal e-mail correspondence*. Tech. rep. Holland Proton Therapy Centre, 2021.

[52] A.R. Schornagel. “Towards high dose rate proton radiation in zebrafish”. In: *TU Delft Repository* (2021).

[53] ThermoFisher Scientific. *How to Select a Secondary Antibody*. 2020. URL: https://www.thermofisher.com/nl/en/home/life-science/antibodies/secondary-antibodies (visited on 06/10/2022).

[54] Medicago. “Phosphate Buffered Saline with Tween™ 20 (PBS-T), pH 7.4”. In: *Smartbuffers* (2011).

[55] Abcam. “Normal Goat Serum”. In: *Product Datasheet* (2022).

[56] David Chall, Joseph Perl. *Topas Documentation*. 2022. URL: https://topas.readthedocs.io/en/latest/getting-started/citation.html.

[57] Bernd Pelster and Brian Bagatto. “7 - Respiration”. In: *Zebrafish*. Ed. by Steve F. Perry et al. Vol. 29. Fish Physiology. Academic Press, 2010, pp. 289–309. DOI: https://doi.org/10.1016/S1546-5098(10)02907-9. URL: https://www.sciencedirect.com/science/article/pii/S1546509810029079.

[58] Douglas G Howe et al. “ZFIN, the Zebrafish Model Organism Database: increased support for mutants and transgenics”. In: *Nucleic acids research* 41.D1 (2012), pp. D854–D860.

[59] Martin J Berger, J S Coursey, M A Zucker, et al. “ESTAR, PSTAR, and ASTAR: computer programs for calculating stopping-power and range tables for electrons, protons, and helium ions (version 1.21)”. In: (1999).

[60] Kristina Rojdev. “Long term lunar radiation degradation of potential lunar habitat composite materials”. PhD thesis. Dec. 2012.

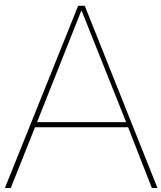

Body of the TopasMC Code

```
############ HEADERS ############
i:So/Disk/NumberOfHistoriesInRun = 10000000
b:Ge/QuitIfOverlapDetected = "True"
i:Ts/ShowHistoryCountAtInterval = 2000
b:Ts/ShowCPUTime = "True"

############ WORLD PARAMETERS ############
d:Ge/World/HLX = 10 cm
d:Ge/World/HLY = 10 cm
d:Ge/World/HLZ = 60 cm
s:Ge/World/Material="Air"
#b:Ge/World/Invisible = "1"

############ WET SLABS ############
s:Ge/slab/Parent = "World"
s:Ge/slab/Type = "Tsbox"
s:Ge/slab/Material = "G4_WATER"
d:Ge/slab/HLX = 6 cm
d:Ge/slab/HLY = 6 cm
d:Ge/slab/HLZ = 4.45 cm
d:Ge/slab/TransZ = -31 cm

############ IMPORT WELLPLATE CODE ############
includeFile = /home/chiel/MEP/WellPlate

############ UNCOMMENT THIS SECTION FOR SOBP CALCULATIONS ############

### Parallel Volumes to inspect SOBP's ###
s:Ge/sobpscorer0/Parent = "World"
s:Ge/sobpscorer0/Type = "TsCylinder"
b:Ge/sobpscorer0/IsParallel = "True"
d:Ge/sobpscorer0/Rmax = 4 mm
d:Ge/sobpscorer0/HL = 5.45 cm
d:Ge/sobpscorer0/TransZ = -32 cm
d:Ge/sobpscorer0/TransX = 0 cm
i:Ge/sobpscorer0/zbins = 200

s:Ge/sobpscorer1/Parent = "World"
s:Ge/sobpscorer1/Type = "TsCylinder"
```

```
b:Ge/sobpscorer1/IsParallel = "True"
d:Ge/sobpscorer1/Rmax = 2 mm
d:Ge/sobpscorer1/HL = 5.45 cm
d:Ge/sobpscorer1/TransZ = -32 cm
d:Ge/sobpscorer1/TransX = 0 cm
i:Ge/sobpscorer1/zbins = 200

s:Ge/sobpscorer2/Parent = "World"
s:Ge/sobpscorer2/Type = "TsCylinder"
b:Ge/sobpscorer2/IsParallel = "True"
d:Ge/sobpscorer2/Rmax = 1 mm
d:Ge/sobpscorer2/HL = 5.45 cm
d:Ge/sobpscorer2/TransZ = -32 cm
d:Ge/sobpscorer2/TransX = 0 cm
i:Ge/sobpscorer2/zbins = 200

s:Ge/sobpscorer3/Parent = "World"
s:Ge/sobpscorer3/Type = "TsCylinder"
b:Ge/sobpscorer3/IsParallel = "True"
d:Ge/sobpscorer3/Rmax = 0.3 mm
d:Ge/sobpscorer3/HL = 5.45 cm
d:Ge/sobpscorer3/TransZ = -32 cm
d:Ge/sobpscorer3/TransX = 0 cm
i:Ge/sobpscorer3/zbins = 200

s:Ge/sobpscorer4/Parent = "World"
s:Ge/sobpscorer4/Type = "TsCylinder"
b:Ge/sobpscorer4/IsParallel = "True"
d:Ge/sobpscorer4/Rmax = 0.1 mm
d:Ge/sobpscorer4/HL = 5.45 cm
d:Ge/sobpscorer4/TransZ = -32 cm
d:Ge/sobpscorer4/TransX = 0 cm
i:Ge/sobpscorer4/zbins = 200

s:Sc/MyScorer1/Quantity                  = "EnergyDeposit"
s:Sc/MyScorer1/Component                 = "sobpscorer0"
s:Sc/MyScorer1/OutputType                = "csv"
s:Sc/MyScorer1/OutputFile = "/home/chiel/topas_output/sobp_energydepsit_4mm"
b:Sc/MyScorer1/OutputToConsole           = "False"
s:Sc/MyScorer1/IfOutputFileAlreadyExists = "Overwrite"
sv:Sc/MyScorer1/Report = 2 "Sum" "Standard_Deviation"

s:Sc/MyScorer2/Quantity                  = "EnergyDeposit"
s:Sc/MyScorer2/Component                 = "sobpscorer1"
s:Sc/MyScorer2/OutputType                = "csv"
s:Sc/MyScorer2/OutputFile = "/home/chiel/topas_output/sobp_energydepsit_2mm"
b:Sc/MyScorer2/OutputToConsole           = "False"
s:Sc/MyScorer2/IfOutputFileAlreadyExists = "Overwrite"
sv:Sc/MyScorer2/Report = 2 "Sum" "Standard_Deviation"

s:Sc/MyScorer3/Quantity                  = "EnergyDeposit"
s:Sc/MyScorer3/Component                 = "sobpscorer2"
s:Sc/MyScorer3/OutputType                = "csv"
s:Sc/MyScorer3/OutputFile = "/home/chiel/topas_output/sobp_energydepsit_1mm"
b:Sc/MyScorer3/OutputToConsole           = "False"
s:Sc/MyScorer3/IfOutputFileAlreadyExists = "Overwrite"
```

```
sv:Sc/MyScorer3/Report = 2 "Sum" "Standard_Deviation"

s:Sc/MyScorer4/Quantity                  = "EnergyDeposit"
s:Sc/MyScorer4/Component                 = "sobpscorer3"
s:Sc/MyScorer4/OutputType                = "csv"
s:Sc/MyScorer4/OutputFile = "/home/chiel/topas_output/sobp_energydepsit_03mm"
b:Sc/MyScorer4/OutputToConsole           = "False"
s:Sc/MyScorer4/IfOutputFileAlreadyExists = "Overwrite"
sv:Sc/MyScorer4/Report = 2 "Sum" "Standard_Deviation"

s:Sc/MyScorer5/Quantity                  = "EnergyDeposit"
s:Sc/MyScorer5/Component                 = "sobpscorer4"
s:Sc/MyScorer5/OutputType                = "csv"
s:Sc/MyScorer5/OutputFile = "/home/chiel/topas_output/sobp_energydepsit_01mm"
b:Sc/MyScorer5/OutputToConsole           = "False"
s:Sc/MyScorer5/IfOutputFileAlreadyExists = "Overwrite"
sv:Sc/MyScorer5/Report = 2 "Sum" "Standard_Deviation"

### Water Phantom after WET slab to get full SOBP ###
s:Ge/extrawater/Parent = "World"
s:Ge/extrawater/Type = "Tsbox"
s:Ge/extrawater/Material = "G4_WATER"
d:Ge/extrawater/HLX = 6 cm
d:Ge/extrawater/HLY = 6 cm
d:Ge/extrawater/HLZ = 1 cm
d:Ge/extrawater/TransZ = -36.45 cm

############ UNCOMMENT THIS SECTION FOR HOMOGENEITY SIMULATIONS ############

### Parallel Volume to Inspect Well (box) ###
#s:Ge/Wellphantombox/Parent = "World"
#s:Ge/Wellphantombox/Type = "TsBox"
#b:Ge/Wellphantombox/IsParallel = "True"
#d:Ge/Wellphantombox/HLX = 4.5 mm
#d:Ge/Wellphantombox/HLY = 4.5 mm
#d:Ge/Wellphantombox/HLZ = 0.9 cm
#d:Ge/Wellphantombox/TransX = 0 cm
#d:Ge/Wellphantombox/TransY = 0 cm
#d:Ge/Wellphantombox/TransZ = -34.45 cm
#i:Ge/Wellphantombox/XBins = 25
#i:Ge/Wellphantombox/YBins = 25
#i:Ge/Wellphantombox/ZBins = 4

#s:Sc/MyScorer2/Quantity                  = "DoseToMedium"
#s:Sc/MyScorer2/Component                 = "Wellphantombox"
#s:Sc/MyScorer2/OutputType                = "csv"
#s:Sc/MyScorer2/OutputFile = "/home/chiel/topas_output/flash_test"
#b:Sc/MyScorer2/OutputToConsole           = "False"
#s:Sc/MyScorer2/IfOutputFileAlreadyExists = "Overwrite"
#sv:Sc/MyScorer2/Report = 2 "Sum" "Standard_Deviation"

############ IMPORT BEAM CHARACTERISTICS ############

### Include beam parameter file ###
#includeFile = /home/chiel/MEP/CONV_beam
includeFile = /home/chiel/MEP/FLASH_beam
```

```
### BeamPosition ###
d:Ge/BeamPosition/TransZ = Ge/World/HLZ m
d:Ge/BeamPosition/RotX = 180. deg
s:Ge/BeamPosition/Parent = "World"
s:Ge/BeamPosition/Type = "Group"

############ GRAPHING (ONLY TO CHECK GEOMETRY) ############

#s:Gr/ViewA/Type = "OpenGL"
#s:Gr/ViewA/Projection  = "Perspective"
#i:Gr/ViewA/WindowSizeX = 900
#i:Gr/ViewA/WindowSizeY = 700
#b:Ts/PauseBeforeQuit = "True"

### Enable GUI ###
#Ts/UseQt = "True"
```

B

Auxiliary Topas Code

B.1. WellPlate

```
### Polystyrene (wellplate material) ###
sv:Ma/Polystyrene/Components = 2 "Carbon" "Hydrogen"
uv:Ma/Polystyrene/Fractions = 2 0.9226 0.0774
d:Ma/Polystyrene/Density = 1.06 g/cm3
d:Ma/Polystyrene/MeanExcitationEnergy = 68 eV

### Resin (lid material) ###
sv:Ma/Resin/Components = 3 "Carbon" "Hydrogen" "Oxygen"
uv:Ma/Resin/Fractions = 3 0.35 0.53 0.12
d:Ma/Resin/Density = 1.22 g/cm3
d:Ma/Resin/MeanExcitationEnergy = 70 eV

### Holder mixture ###
b:Ma/holder/BuildFromMaterials = "True"
sv:Ma/holder/Components = 2 "Air" "Polystyrene"
uv:Ma/holder/Fractions = 2 .75 .25
d:Ma/holder/Density = .25 g/cm3

### Holder surrounding ###
s:Ge/surrounding/Parent = "slab"
s:Ge/surrounding/Type = "Tsbox"
s:Ge/surrounding/Material = "holder"
d:Ge/surrounding/HLX = 6 cm
d:Ge/surrounding/HLY = 6 cm
d:Ge/surrounding/HLZ = 1 cm
d:Ge/surrounding/TransZ = -3.45 cm
s:Ge/surrounding/Color = "Blue"

### Well plate parent ###
s:Ge/WellPlate/Parent = "surrounding"
s:Ge/WellPlate/Type = "Tsbox"
s:Ge/WellPlate/Material = "Air"
d:Ge/WellPlate/HLX = 1.35 cm
d:Ge/WellPlate/HLY = 1.35 cm
d:Ge/WellPlate/HLZ = 0.9 cm
d:Ge/WellPlate/TransZ = 0 cm
s:Ge/WellPlate/Color = "Green"
```

```
### Resin Lid ###
s:Ge/WellLid/Parent = "surrounding"
s:Ge/WellLid/Type = "Tsbox"
s:Ge/WellLid/Material = "Resin"
d:Ge/WellLid/HLX = 1.35 cm
d:Ge/WellLid/HLY = 1.35 cm
d:Ge/WellLid/HLZ = 0.5 mm
d:Ge/WellLid/TransZ = 0.95 cm

### Wellplate bottom ###
s:Ge/Wellbottom/Parent = "surrounding"
s:Ge/Wellbottom/Type = "Tsbox"
s:Ge/Wellbottom/Material = "Polystyrene"
d:Ge/Wellbottom/HLX = 1.35 cm
d:Ge/Wellbottom/HLY = 1.35 cm
d:Ge/Wellbottom/HLZ = 0.5 mm
d:Ge/Wellbottom/TransZ = -0.95 cm

### Well cases ###

s:Ge/Wellc1/Parent = "WellPlate"
s:Ge/Wellc1/Type = "TsCylinder"
s:Ge/Wellc1/Material = "Polystyrene"
d:Ge/Wellc1/Rmin = 4 mm
d:Ge/Wellc1/Rmax = 4.5 mm
d:Ge/Wellc1/HL = 0.9 cm
d:Ge/Wellc1/TransX = 0 cm
d:Ge/Wellc1/TransY = 0 cm
s:Ge/Wellc1/Color = "Green"

s:Ge/Wellc2/Parent = "WellPlate"
s:Ge/Wellc2/Type = "TsCylinder"
s:Ge/Wellc2/Material = "Polystyrene"
d:Ge/Wellc2/Rmin = 4 mm
d:Ge/Wellc2/Rmax = 4.5 mm
d:Ge/Wellc2/HL = 0.9 cm
d:Ge/Wellc2/TransX = -0.9 cm
d:Ge/Wellc2/TransY = 0 cm
s:Ge/Wellc2/Color = "Green"

s:Ge/Wellc3/Parent = "WellPlate"
s:Ge/Wellc3/Type = "TsCylinder"
s:Ge/Wellc3/Material = "Polystyrene"
d:Ge/Wellc3/Rmin = 4 mm
d:Ge/Wellc3/Rmax = 4.5 mm
d:Ge/Wellc3/HL = 0.9 cm
d:Ge/Wellc3/TransX = 0.9 cm
d:Ge/Wellc3/TransY = 0 cm
s:Ge/Wellc3/Color = "Green"

s:Ge/Wellc4/Parent = "WellPlate"
s:Ge/Wellc4/Type = "TsCylinder"
s:Ge/Wellc4/Material = "Polystyrene"
d:Ge/Wellc4/Rmin = 4 mm
d:Ge/Wellc4/Rmax = 4.5 mm
d:Ge/Wellc4/HL = 0.9 cm
```

```
d:Ge/Wellc4/TransX = 0 cm
d:Ge/Wellc4/TransY = 0.9 cm
s:Ge/Wellc4/Color = "Green"

s:Ge/Wellc5/Parent = "WellPlate"
s:Ge/Wellc5/Type = "TsCylinder"
s:Ge/Wellc5/Material = "Polystyrene"
d:Ge/Wellc5/Rmin = 4 mm
d:Ge/Wellc5/Rmax = 4.5 mm
d:Ge/Wellc5/HL = 0.9 cm
d:Ge/Wellc5/TransX = -0.9 cm
d:Ge/Wellc5/TransY = 0.9 cm
s:Ge/Wellc5/Color = "Green"

s:Ge/Wellc6/Parent = "WellPlate"
s:Ge/Wellc6/Type = "TsCylinder"
s:Ge/Wellc6/Material = "Polystyrene"
d:Ge/Wellc6/Rmin = 4 mm
d:Ge/Wellc6/Rmax = 4.5 mm
d:Ge/Wellc6/HL = 0.9 cm
d:Ge/Wellc6/TransX = 0.9 cm
d:Ge/Wellc6/TransY = 0.9 cm
s:Ge/Wellc6/Color = "Green"

s:Ge/Wellc7/Parent = "WellPlate"
s:Ge/Wellc7/Type = "TsCylinder"
s:Ge/Wellc7/Material = "Polystyrene"
d:Ge/Wellc7/Rmin = 4 mm
d:Ge/Wellc7/Rmax = 4.5 mm
d:Ge/Wellc7/HL = 0.9 cm
d:Ge/Wellc7/TransX = 0 cm
d:Ge/Wellc7/TransY = -0.9 cm
s:Ge/Wellc7/Color = "Green"

s:Ge/Wellc8/Parent = "WellPlate"
s:Ge/Wellc8/Type = "TsCylinder"
s:Ge/Wellc8/Material = "Polystyrene"
d:Ge/Wellc8/Rmin = 4 mm
d:Ge/Wellc8/Rmax = 4.5 mm
d:Ge/Wellc8/HL = 0.9 cm
d:Ge/Wellc8/TransX = -0.9 cm
d:Ge/Wellc8/TransY = -0.9 cm
s:Ge/Wellc8/Color = "Green"

s:Ge/Wellc9/Parent = "WellPlate"
s:Ge/Wellc9/Type = "TsCylinder"
s:Ge/Wellc9/Material = "Polystyrene"
d:Ge/Wellc9/Rmin = 4 mm
d:Ge/Wellc9/Rmax = 4.5 mm
d:Ge/Wellc9/HL = 0.9 cm
d:Ge/Wellc9/TransX = 0.9 cm
d:Ge/Wellc9/TransY = -0.9 cm
s:Ge/Wellc9/Color = "Green"

### Wells ###
```

```
s:Ge/Well1/Parent = "WellPlate"
s:Ge/Well1/Type = "TsCylinder"
s:Ge/Well1/Material = "G4_WATER"
d:Ge/Well1/Rmax = 4 mm
d:Ge/Well1/HL = 0.9 cm
d:Ge/Well1/TransX = 0 cm
d:Ge/Well1/TransY = 0 cm

s:Ge/Well2/Parent = "WellPlate"
s:Ge/Well2/Type = "TsCylinder"
s:Ge/Well2/Material = "Air"
d:Ge/Well2/Rmax = 4 mm
d:Ge/Well2/HL = 0.9 cm
d:Ge/Well2/TransX = -0.9 cm
d:Ge/Well2/TransY = 0 cm

s:Ge/Well3/Parent = "WellPlate"
s:Ge/Well3/Type = "TsCylinder"
s:Ge/Well3/Material = "Air"
d:Ge/Well3/Rmax = 4 mm
d:Ge/Well3/HL = 0.9 cm
d:Ge/Well3/TransX = 0.9 cm
d:Ge/Well3/TransY = 0 cm

s:Ge/Well4/Parent = "WellPlate"
s:Ge/Well4/Type = "TsCylinder"
s:Ge/Well4/Material = "Air"
d:Ge/Well4/Rmax = 4 mm
d:Ge/Well4/HL = 0.9 cm
d:Ge/Well4/TransX = 0 cm
d:Ge/Well4/TransY = 0.9 cm

s:Ge/Well5/Parent = "WellPlate"
s:Ge/Well5/Type = "TsCylinder"
s:Ge/Well5/Material = "Air"
d:Ge/Well5/Rmax = 4 mm
d:Ge/Well5/HL = 0.9 cm
d:Ge/Well5/TransX = -0.9 cm
d:Ge/Well5/TransY = 0.9 cm

s:Ge/Well6/Parent = "WellPlate"
s:Ge/Well6/Type = "TsCylinder"
s:Ge/Well6/Material = "G4_WATER"
d:Ge/Well6/Rmax = 4 mm
d:Ge/Well6/HL = 0.9 cm
d:Ge/Well6/TransX = 0.9 cm
d:Ge/Well6/TransY = 0.9 cm

s:Ge/Well7/Parent = "WellPlate"
s:Ge/Well7/Type = "TsCylinder"
s:Ge/Well7/Material = "Air"
d:Ge/Well7/Rmax = 4 mm
d:Ge/Well7/HL = 0.9 cm
d:Ge/Well7/TransX = 0 cm
d:Ge/Well7/TransY = -0.9 cm
```

```
s:Ge/Well8/Parent = "WellPlate"
s:Ge/Well8/Type = "TsCylinder"
s:Ge/Well8/Material = "Air"
d:Ge/Well8/Rmax = 4 mm
d:Ge/Well8/HL = 0.9 cm
d:Ge/Well8/TransX = -0.9 cm
d:Ge/Well8/TransY = -0.9 cm

s:Ge/Well9/Parent = "WellPlate"
s:Ge/Well9/Type = "TsCylinder"
s:Ge/Well9/Material = "Air"
d:Ge/Well9/Rmax = 4 mm
d:Ge/Well9/HL = 0.9 cm
d:Ge/Well9/TransX = 0.9 cm
d:Ge/Well9/TransY = -0.9 cm
```

B.2. CONV_beam

```
### Beam ###

s:So/Disk/Type = "Beam"
s:So/Disk/Component = "BeamPosition"
s:So/Disk/BeamParticle = "proton"
s:So/Disk/BeamEnergySpectrumType = "Continuous"

u:So/Disk/BeamEnergySpread = 0.94
s:So/Disk/BeamPositionDistribution = "Flat"
s:So/Disk/BeamAngularDistribution = "Gaussian"
d:So/Disk/BeamAngularCutoffX = 90 deg
d:So/Disk/BeamAngularCutoffY = 90 deg
s:So/Disk/BeamPositionCutoffShape = "Rectangle"
d:So/Disk/BeamAngularSpreadX = 0.0027 rad
d:So/Disk/BeamAngularSpreadY = 0.0032 rad
d:So/Disk/BeamPositionSpreadX = 0.27 cm
d:So/Disk/BeamPositionSpreadY = 0.21 cm
d:So/Disk/BeamPositionCutoffX = 1.35 cm
d:So/Disk/BeamPositionCutoffY = 1.35 cm

### Include Energies ###
includeFile = /home/chiel/MEP/energies
```

B.3. FLASH_beam

```
### Beam ###

s:So/Disk/Type = "Beam"
s:So/Disk/Component = "BeamPosition"
s:So/Disk/BeamParticle = "proton"
s:So/Disk/BeamEnergySpectrumType = "Continuous"

u:So/Disk/BeamEnergySpread = 0.8
s:So/Disk/BeamPositionDistribution = "Gaussian"
s:So/Disk/BeamAngularDistribution = "Gaussian"
d:So/Disk/BeamAngularCutoffX = 90 deg
d:So/Disk/BeamAngularCutoffY = 90 deg
```

```
s:So/Disk/BeamPositionCutoffShape = "Ellipse"
d:So/Disk/BeamAngularSpreadX = 0.00275 rad
d:So/Disk/BeamAngularSpreadY = 0.0032 rad
d:So/Disk/BeamPositionSpreadX = 0.275 cm
d:So/Disk/BeamPositionSpreadY = 0.21 cm
d:So/Disk/BeamPositionCutoffX = 7 cm
d:So/Disk/BeamPositionCutoffY = 7 cm

### Include Energies ###
includeFile = /home/chiel/MEP/energies
```

B.4. energies

```
dv:So/Disk/BeamEnergySpectrumValues = 99 87.8172202020202
88.2212606060606        88.6253010101010        89.0293414141414
89.4333818181818        89.8374222222222        90.2414626262626
90.6455030303030        91.0495434343435        91.4535838383838
91.8576242424243        92.2616646464646        92.6657050505051
93.0697454545455        93.4737858585859        93.8778262626263
94.2818666666667        94.6859070707071        95.0899474747475
95.4939878787879        95.8980282828283        96.3020686868687
96.7061090909091        97.1101494949495        97.5141898989899
97.9182303030303        98.3222707070707        98.7263111111111
99.1303515151515        99.5343919191919        99.9384323232323
100.342472727273        100.746513131313        101.150553535354
101.554593939394        101.958634343434        102.362674747475
102.766715151515        103.170755555556        103.574795959596
103.978836363636        104.382876767677        104.786917171717
105.190957575758        105.594997979798        105.999038383838
106.403078787879        106.807119191919        107.211159595960
107.615200000000        108.019240404040        108.423280808081
108.827321212121        109.231361616162        109.635402020202
110.039442424242        110.443482828283        110.847523232323
111.251563636364        111.655604040404        112.059644444444
112.463684848485        112.867725252525        113.271765656566
113.675806060606        114.079846464646        114.483886868687
114.887927272727        115.291967676768        115.696008080808
116.100048484849        116.504088888889        116.908129292929
117.312169696970        117.716210101010        118.120250505051
118.524290909091        118.928331313131        119.332371717172
119.736412121212        120.140452525253        120.544492929293
120.948533333333        121.352573737374        121.756614141414
122.160654545455        122.564694949495        122.968735353535
123.372775757576        123.776816161616        124.180856565657
124.584896969697        124.988937373737        125.392977777778
125.797018181818        126.201058585859        126.605098989899
127.009139393939        127.413179797980 MeV

uv:So/Disk/BeamEnergySpectrumWeights = 99 1.01348954585533e-05
4.05395818342134e-05    4.05395818342134e-05    1.01348954585533e-05
5.06744772927667e-05    4.05395818342134e-05    3.04046863756600e-05
0       2.02697909171067e-05    2.02697909171067e-05
8.10791636684268e-05    0.000121618745502640    0.000344586445590814
0.000628363518430307    0.00105402912768955     0.00171279733249552
0.00251345407372123     0.00382085558787461     0.00532082011574051
0.00635457945251295     0.00736806899836828     0.00803697209863280
```

```
0.00827007469417953     0.00809778147138412     0.00764171117574922
0.00693226849365049     0.00652687267530835     0.00664849142081099
0.00642552372072282     0.00715523619373866     0.00749982263932948
0.00760117159391501     0.00855385176701902     0.00820926532142821
0.00871601009435588     0.00863493093068745     0.00854371687156047
0.00859439134885324     0.00907073143540524     0.00910113612178090
0.00980044390842108     0.00981057880387964     0.00998287202667504
0.0106619100223981      0.0105200214859784      0.0105301563814369
0.0114220271817896      0.0121821443411811      0.0117868834182975
0.0119389068501758      0.0123443026685180      0.0123240328776009
0.0123544375639765      0.0130638802460753      0.0137530531372569
0.0154658504697524      0.0161246186745584      0.0167732519839058
0.0184759144209428      0.0196211576077593      0.0194995388622566
0.0195096737577152      0.0196819669805106      0.0187495565983237
0.0209995033901225      0.0246987402324945      0.0324924748401220
0.0427793937305537      0.0522352511933839      0.0614478711652089
0.0642755069981453      0.0583871327367258      0.0474617154324053
0.0348640403774235      0.0220028580405193      0.0118882323728831
0.00619242112517609     0.00254385876009689     0.0010236244413138
9       0.000354721341049367    0.000101348954585533    1.0134
8954585533e-05  2.02697909171067e-05    0       0       0       0       0
0       0       0       0       0       0
0       0       0       0       0
```

C

Python Code to plot dose profiles and calculate homogeneity

```
import numpy as np
import matplotlib.pyplot as plt

# Parameters
xcol = 0
ycol = 1
zcol = 2
score = 3
std = 4
myslice = 3
platesize = 9
circlesize = 8

# File import
#path = '/home/chiel/topas_output/smallwellbox_conv.csv'
path = '/home/chiel/topas_output/flash_10^7.csv'
data = np.genfromtxt(path, delimiter=',')

# Find hits at relevant slice
myZ = np.where(data[:,zcol]==myslice)
hits = data[myZ,:]

# Finding nr of bins
xbins = int(np.amax(hits[0,:,xcol]) + 1)
ybins = int(np.amax(hits[0,:,ycol]) + 1)

# Disregard air voxels
well_edge_squared = (xbins/platesize*circlesize/2)**2
no_air_data = np.where((data[:,xcol]-xbins/2+1)**2+
(data[:,ycol]-ybins/2+1)**2 <= well_edge_squared)
wellU = data[no_air_data]

# Defining x, y and z for convenience
x = np.linspace(0, platesize, xbins)
y = np.linspace(0, platesize, ybins)
z = hits[0,:,score]
```

```
# Heatmap
X, Y = np.meshgrid(x,y)
Z = np.reshape(z,(xbins,ybins))

# Plot colormeshc
maxscore = np.amax(data[:,score])
minscore = np.amin(data[:,score])
plt.pcolor(X, Y, Z, shading='flat', vmin=minscore, vmax=maxscore)

# Add well outline
well_inner = plt.Circle((platesize/2, platesize/2), circlesize/2,
fill=False, color='r')
well_outer = plt.Circle((platesize/2, platesize/2), platesize/2,
fill=False, color='r')
plt.gca().add_patch(well_inner)
plt.gca().add_patch(well_outer)

# Figure properties
plt.colorbar()
plt.axis('square')
plt.xlabel("x position (mm)")
plt.ylabel("y position (mm)")
```

D

MAX-projections of the images used to generate figure 4.4

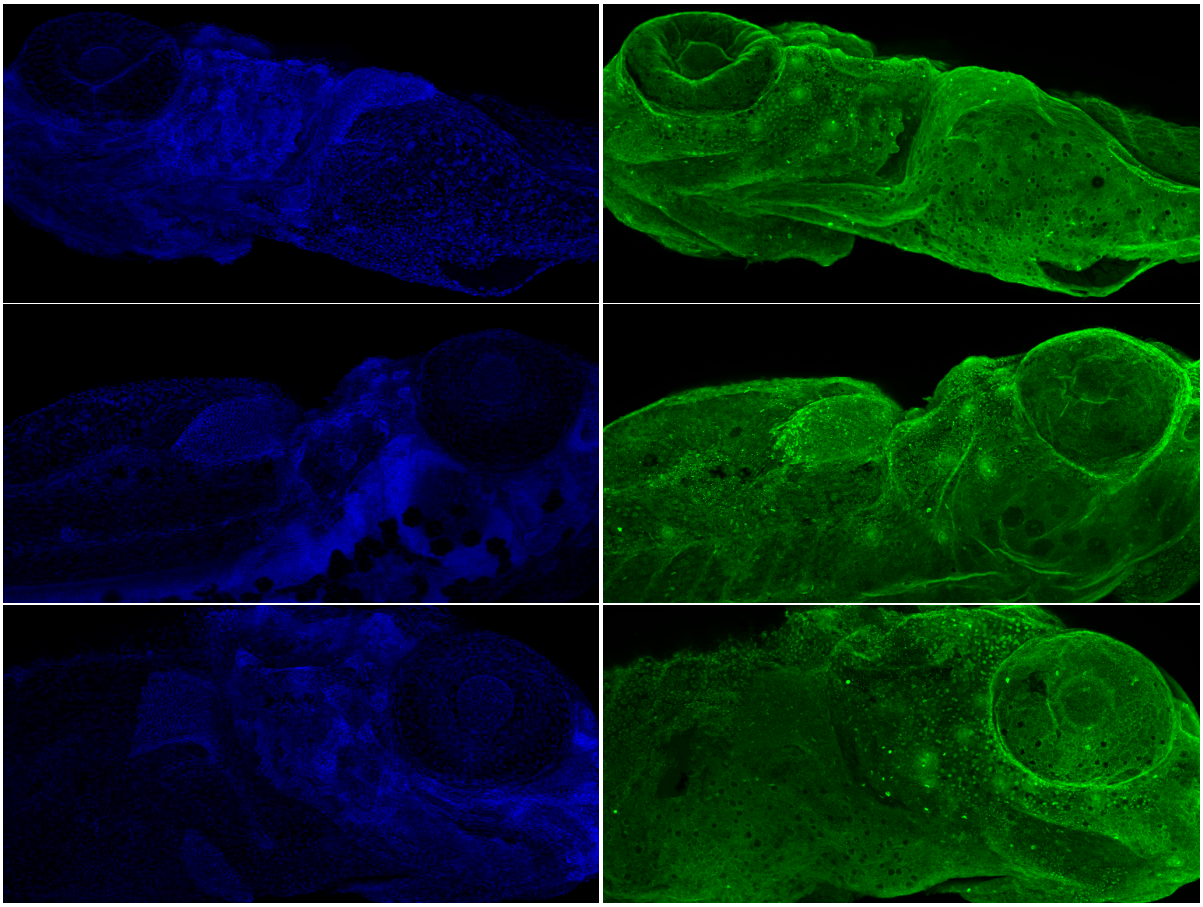

Figure D.1: 15 Gy Hypoxic, CONV radiation. Left: DAPI channel. Right: γ-H2AX channel.

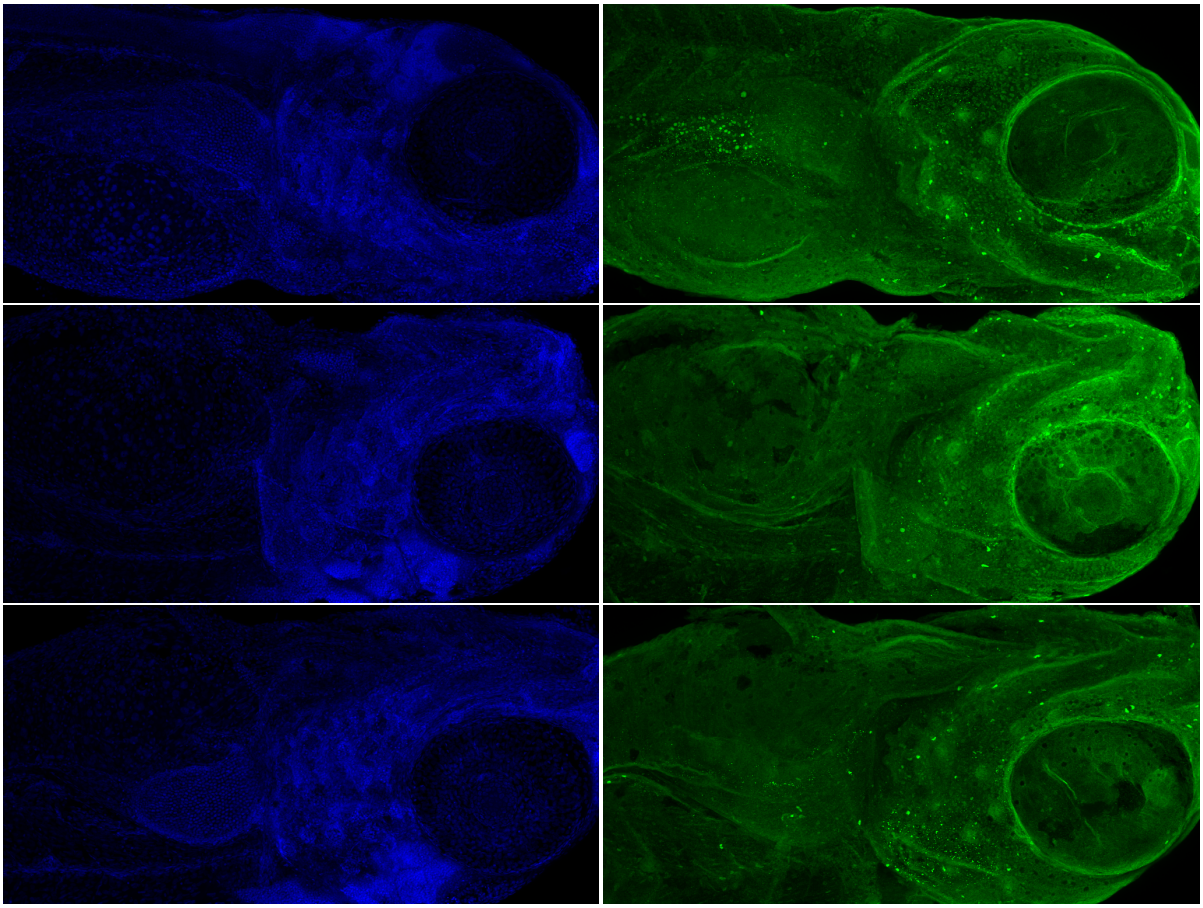

Figure D.2: 15 Gy Normoxic, CONV radiation. Left: DAPI channel. Right: γ-H2AX channel.

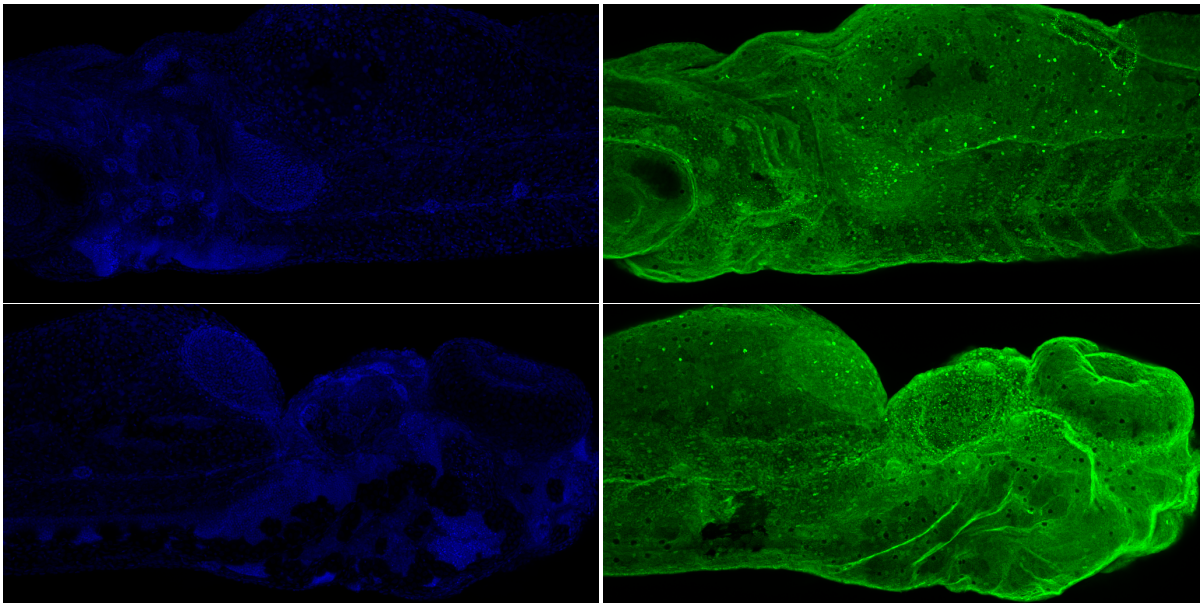

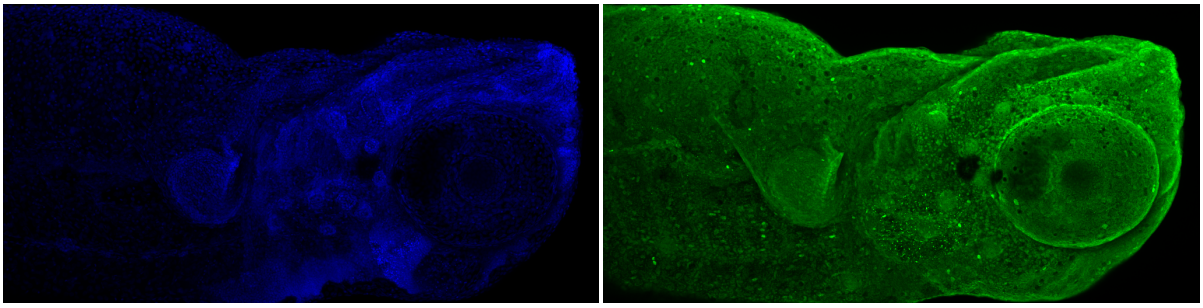

Figure D.3: 15 Gy Normoxic, FLASH radiation. Left: DAPI channel. Right: γ-H2AX channel.

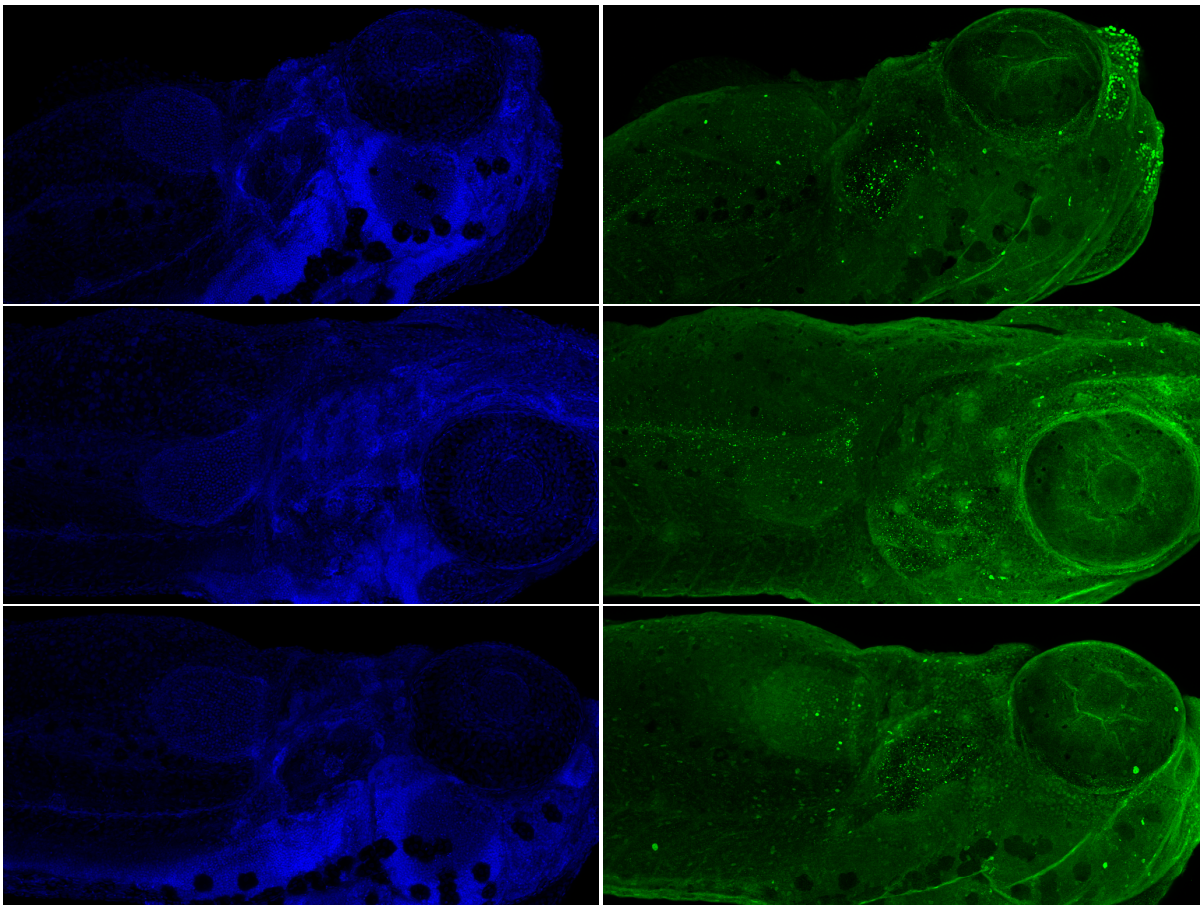

Figure D.4: 25 Gy Hypoxic, CONV radiation. Left: DAPI channel. Right: γ-H2AX channel.

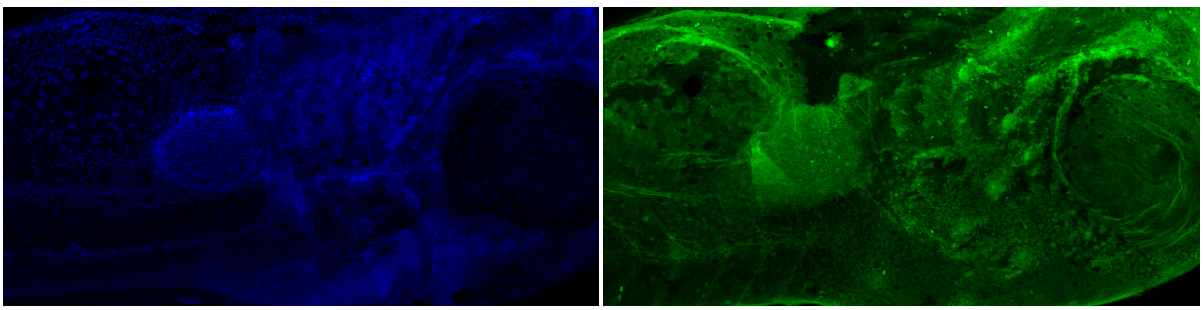

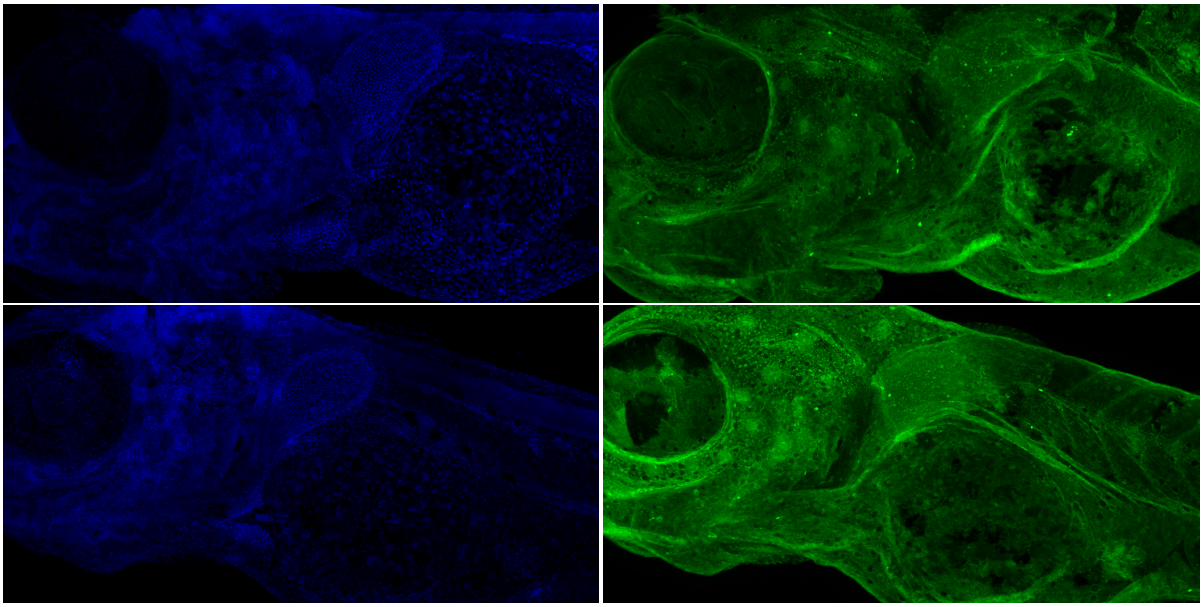

Figure D.5: 25 Gy Normoxic, CONV radiation. Left: DAPI channel. Right: γ-H2AX channel.

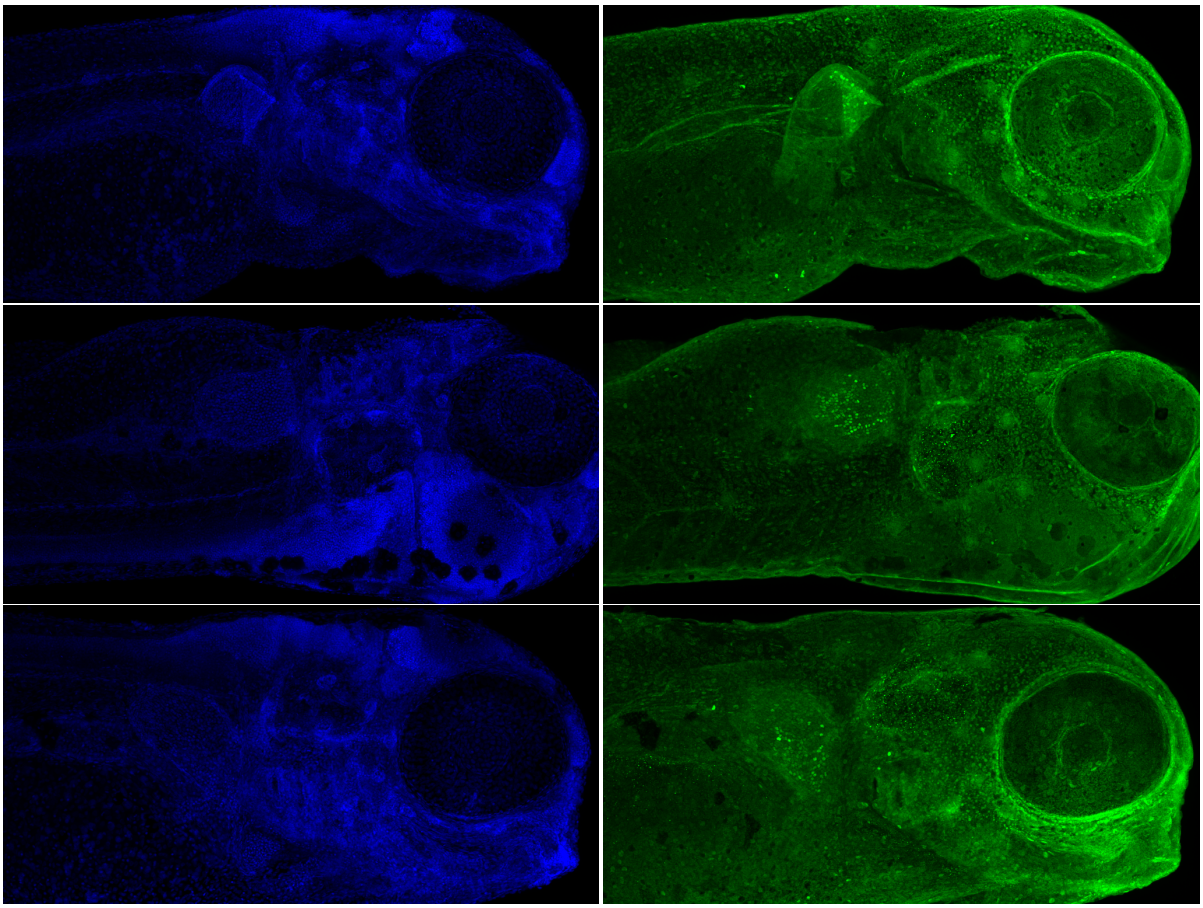

Figure D.6: 25 Gy Normoxic, FLASH radiation. Left: DAPI channel. Right: γ-H2AX channel.